JOURNAL OF GEOPHYSICAL RESEARCH, VOL. 115, B03416, doi:10.1029/2009JB006383, 2010

Effect of clay content and mineralogy on frictional sliding behavior of simulated gouges: Binary and ternary mixtures of quartz, illite, and montmorillonite

Sheryl Tembe,[1] David A. Lockner,[2] and Teng-Fong Wong[3]

Received 13 February 2009; revised 31 August 2009; accepted 28 October 2009; published 24 March 2010.

[1] We investigated the frictional sliding behavior of simulated quartz-clay gouges under stress conditions relevant to seismogenic depths. Conventional triaxial compression tests were conducted at 40 MPa effective normal stress on saturated saw cut samples containing binary and ternary mixtures of quartz, montmorillonite, and illite. In all cases, frictional strengths of mixtures fall between the end-members of pure quartz (strongest) and clay (weakest). The overall trend was a decrease in strength with increasing clay content. In the illite/quartz mixture the trend was nearly linear, while in the montmorillonite mixtures a sigmoidal trend with three strength regimes was noted. Microstructural observations were performed on the deformed samples to characterize the geometric attributes of shear localization within the gouge layers. Two micromechanical models were used to analyze the critical clay fractions for the two-regime transitions on the basis of clay porosity and packing of the quartz grains. The transition from regime 1 (high strength) to 2 (intermediate strength) is associated with the shift from a stress-supporting framework of quartz grains to a clay matrix embedded with disperse quartz grains, manifested by the development of P-foliation and reduction in Riedel shear angle. The transition from regime 2 (intermediate strength) to 3 (low strength) is attributed to the development of shear localization in the clay matrix, occurring only when the neighboring layers of quartz grains are separated by a critical clay thickness. Our mixture data relating strength degradation to clay content agree well with strengths of natural shear zone materials obtained from scientific deep drilling projects.

Citation: Tembe, S., D. A. Lockner, and T.-F. Wong (2010), Effect of clay content and mineralogy on frictional sliding behavior of simulated gouges: Binary and ternary mixtures of quartz, illite, and montmorillonite, *J. Geophys. Res.*, *115*, B03416, doi:10.1029/2009JB006383.

1. Introduction

[2] The mechanical strength and stability behavior of a fault system depend on the complex interaction between numerous physical and chemical parameters including mineral composition, hydraulic properties (e.g., saturation, pore fluid composition, and permeability), state of stress, and partitioning of strain in the country rock and gouge layer. One of the most important hydromechanical properties of the gouge is the coefficient of friction, defined as the ratio of shear stress to normal stress acting on the fault. Laboratory studies for a variety of rocks and minerals show the frictional strength has an approximately linear dependence on normal stress and that the peak friction coefficient typically ranges from 0.6 to 0.85 [*Byerlee*, 1978]. Exceptions to this trend are platy alteration and hydrated minerals, some of which can be significantly weaker than quartzo-feldspathic materials [*Lockner and Beeler*, 2002; *Moore and Lockner*, 2004, 2007].

[3] In recent years, a number of drilling projects have been conducted to retrieve core samples from seismogenic systems in a variety of tectonic settings. Systematic mineralogical characterization of such core samples from the San Andreas Fault Observatory at Depth (SAFOD) [*Solum et al.*, 2006], Taiwan Chelungpu-fault Drilling Project (TCDP) [*Kuo et al.*, 2005] as well as Ocean Drilling Program (ODP) sites in the Nankai trough [*Underwood et al.*, 1993; *Steurer and Underwood*, 2003; *Wilson et al.*, 2003] and Cascadia basin [*Underwood*, 2002] has underscored the pervasive occurrence of clay minerals in the vicinity of fault zones and décollements. In a shear zone located at 2551 m (measured depth (MD)) penetrated during SAFOD phase 2, the retrieved cuttings have weight percentage of clay (made up of illite, chlorite, and mixed montmorillonite/illite) up to 57% and friction coefficient values as low as 0.30 [*Solum et al.*, 2006; *Tembe et al.*, 2006; *Morrow et al.*, 2007]. In the Nankai trough, the décollement sediments at ODP Sites 808 [*Underwood et al.*, 1993]

[1]Institute for Soil Mechanics and Rock Mechanics, Karlsruhe Institute of Technology, Karlsruhe, Germany.
[2]U.S. Geological Survey, Menlo Park, California, USA.
[3]Department of Geosciences, State University of New York at Stony Brook, Stony Brook, New York, USA.

0148-0227/10/2009JB006383

and 1174 [*Steurer and Underwood*, 2003] have clay contents up to 80% and friction coefficients ranging from 0.16 to 0.24 [*Kopf and Brown*, 2003].

[4] In light of these findings, it is therefore of fundamental importance in earthquake mechanics to have a more comprehensive understanding of how clay mineralogy and content influence the frictional strength and stability behavior of fault gouge, which is typically a mixture of siliciclastic and clay minerals. To be applicable to tectonic settings, laboratory studies should be conducted preferably at stress conditions compatible to those at seismogenic depths. However, most systematic studies of this important question have been conducted in soil mechanics at relatively low stresses (about 1 MPa), which are pertinent to geotechnical problems related to slope stability and hazard assessment [e.g., *Skempton*, 1964; *Lupini et al.*, 1981]. The extent to which these results can be extrapolated to higher stresses is somewhat unclear.

[5] In the fourth Rankine Lecture, *Skempton* [1964] critically reviewed the soil mechanics data and postulated a general correlation between the saturated residual friction and clay fraction, that is manifested by a relatively smooth transition with increasing clay content from a high-friction coefficient (corresponding to that of a granular soil) to a minimum coefficient (related to sliding between low-friction clay particles). This transition was elaborated by *Lupini et al.* [1981] who observed that the overall degradation of frictional strength can be separated into three sequential regimes: (1) As the clay content increases up to 25% or so, a very moderate reduction of frictional strength would occur; (2) as the clay content further increases up to about 70%, the frictional strength would decrease significantly; and (3) as the soil evolves to become 100% clay, the frictional strength would again decrease rather moderately to approach a minimum value. They referred to these three regimes as "turbulent shear," "transitional," and "sliding shear," respectively. *Brown et al.* [2003] concluded that similar regimes can be identified in their low-stress data for ODP samples from Nankai as well as the high-stress data of *Logan and Rauenzahn* [1987] on a binary mixture of quartz and montmorillonite. This issue was revisited in two recent studies of binary mixtures at relatively high normal stress. *Takahashi et al.* [2007] argued that their data for a montmorillonite/quartz mixture followed a somewhat different trend, with the frictional strength decreasing with increasing clay content along two linear segments separated by a pronounced drop at a clay fraction of about 50%. In contrast, *Crawford et al.* [2008] concluded that their data for kaolinite/quartz mixtures were in basic agreement with the three-regime model of *Lupini et al.* [1981].

[6] Motivated by these observations, we undertook this study to resolve a series of related questions. Is the three-regime model developed by *Lupini et al.* [1981] necessary or appropriate for describing mixed gouge rheology at effective normal stress applicable to seismogenic depths? The data set of *Takahashi et al.* [2007] that is in apparent discrepancy with most other studies stands out as the one where shear strength was picked at the shortest slip distance = 2.2 mm. How do empirical strength mixing laws depend on slip distance? To clarify the influence of slip distance, we conducted systematic measurements of the frictional strength and hardening behavior to slip distances in excess of 9 mm. Although fault gouges commonly contain more than one clay mineral, most previous studies focused on binary mixture of quartz and a single clay mineral. Do these regimes of frictional strength degradation also occur in a simulated gouge made up of quartz and mixed clay minerals? Do three-component mixtures behave in fundamentally different ways than two-component mixtures? Is the evolution of frictional strength with clay content in such a synthetic mixture manifested by distinct microstructural signatures and are they comparable to those observed in natural soils and fault gouge? To study these questions, we conducted conventional triaxial compression tests on saturated saw cut samples containing binary and ternary gouge mixtures composed of quartz, montmorillonite, and illite. Microstructural observations were also performed on the deformed samples to characterize the geometric attributes of shear localization within the gouge layers.

2. Methodology

2.1. Sample Description and Preparation

[7] Simulated gouge mixtures used in this study were prepared from quartz, montmorillonite, and illite minerals. The quartz powder was commercially acquired Ottawa sand (>99% purity) that was crushed and sieved. Laser particle size analysis showed the size distribution to be skewed with 90% of the particles finer than 175 μm and modal grain size of 140 μm (Figure 1a). A backscattered scanning electron microscope (SEM) image (Figure 1a, inset) of the starting material showed the grains to be angular.

[8] The montmorillonite clay was a commercially obtained sodium bentonite powder (Volclay MPS-1), the same used by *Moore and Lockner* [2007]. It has the chemical composition $Na_{0.3}(Fe^{+2}, Mg)_{0.3}(Al, Fe^{+3})_{1.7}Si_4O_{10}(OH)_2 \cdot nH_2O$, with 94% of the grains being finer than 3 μm, although agglomerated particles may be several time larger (Figure 1b). To remove adsorbed water, the smectite material was dried in a vacuum oven at 100°C for 18 h before being weighed and incorporated into a mixture.

[9] High purity illite is difficult to obtain commercially so often a clay-bearing shale is employed [*Moore et al.*, 1989; *Morrow et al.*, 1992; *Brown et al.*, 2003; *Saffer and Marone*, 2003; *Ikari et al.*, 2009]. Likewise, our illite was derived from Cambrian shale from Silver Hill, Montana supplied by Clay Minerals Society as Imt-1. The shale was comprised predominantly of the disordered monoclinic illite polytype and contained 10–15 wt.% of quartz impurities. Two procedures were employed for preparation of the illite gouge. The first method was to crush and pass the shale through a 325-mesh sieve to obtain particle sizes of <43 μm for use in the mixtures (Figure 1c). In mixtures using illite obtained by this method, it was assumed that the material had a starting quartz content of 12.5 ± 2.5 wt.% and the amount of quartz added was adjusted accordingly. The second procedure was to attain higher purity illite separate from the disaggregated shale by extracting the clay particle size fraction (<5 μm) through gravity settling in a water column. Since this second method can be time consuming and yields limited quantities, only enough material was prepared for the illite end-member experiment. X-ray diffraction (XRD) analysis of the end product showed that the majority of the impurities had been eliminated leaving a relatively pure illite phase (>95%).

[10] While it is more convenient to analyze the packing of a sand/clay mixture in terms of the volumetric clay fraction, accurate determination of this value in a small sample can be

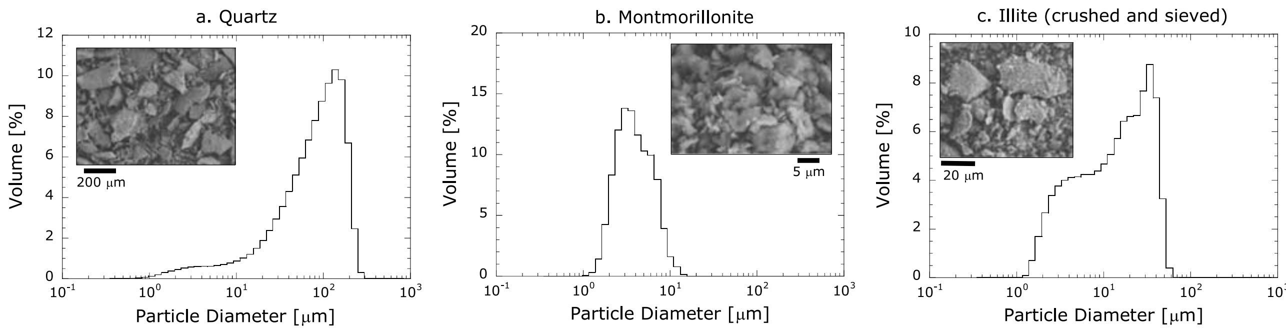

Figure 1. Particle size distribution for (a) quartz, (b) montmorillonite, and (c) illite starting materials. Insets show backscattered SEM images of undeformed material.

problematic. A less ambiguous and widely used property would be the gravimetric clay fraction, which can then be converted to the volumetric component if the constituent grain densities are known. Our sample gouges were prepared from gravimetric mixtures of the dry mineral powders. Altogether five binary mixtures of montmorillonite/quartz, four of illite/quartz, and six ternary mixtures were investigated. The ternary system used equal parts of montmorillonite and illite clays by weight to make up the bulk clay mineral fraction of the mixture before incorporating the quartz. The compositions of the sample gouges are complied in Table 1.

2.2. Experimental Procedure

[11] Frictional sliding experiments were conducted at room temperature in the conventional triaxial configuration on cylindrical forcing blocks (2.54 cm diameter) containing saw cuts inclined at 30° and filled with 1 mm thick simulated gouge layers (Figure 2) and deformed at 40 MPa effective normal stress. The dry mixture was first prepared as a thick paste with deionized water, which was spread onto the saw cut face of the upper forcing block, and then sandwiched by the lower block. To ensure good pore pressure communication between the gouge layer and the external pore pressure system, the upper driving block was either a porous Berea sandstone (20% porosity and high permeability of about 10^{-13} m^2) or for strong, high quartz-content gouges, a Westerly granite block that contained a small hole drilled along the sample axis. The lower driving block was low-porosity (<1%) granite to minimize pore water storage and therefore pore pressure transients that might be generated during rapid stress changes. The assembled saw cut sample was first jacketed with a heat shrinkable polyolefin tubing (0.9 mm wall thickness) to hold the blocks and gouge together and then dried in a vacuum oven at 80°C for a minimum of 4 h. The dried sample was then inserted into a soft polyurethane jacket before being placed in the pressure vessel and hydrostatically loaded to a confining pressure of 41 MPa. Since the gouge layer applied to the saw cut initially contained 50%–60% water, application of confining pressure without pre-drying the sample could result in mobilization of the gouge with undesired consequences. Pre-dried gouge, however, would remain in place during application of confining pressure but would maintain significant porosity (i.e., subsequent shearing would result in gouge compaction).

Table 1. Description of Samples Studied[a]

Sample	Gouge Composition (wt %)			Coefficient of Friction			Hardening Rate (2.00–7.98 mm) $h = \Delta\mu/(\Delta s/t)$	Relative Hardening Rate $h/\mu_{4.00\ \mathrm{mm}}$	Thin Section	Texture (From Figure 7)
	Montmorillonite	Illite	Quartz	2.00 mm	4.00 mm	7.98 mm				
Q 100	0	0	100	0.664	0.698	0.749	0.0120	0.0172	–	–
M 5	5	0	95	0.651	0.705	0.734	0.0106	0.0150	X	A
M 15	15	0	85	0.627	0.647	0.679	0.0080	0.0123	X	A
M 25	25	0	75	0.455	0.476	0.503	0.0057	0.0120	X	B
M 50	50	0	50	0.211	0.237	0.264	0.0070	0.0296	X	C
M 75	75	0	25	0.161	0.165	0.193	0.0042	0.0253	X	C
M 100	100	0	0	0.118	0.129	0.126	–	–	Poor	–
I 15	0	15	85	0.634	0.671	0.726	0.0148	0.0221	–	–
I 25	0	25	75	0.552	0.602	0.655	0.0139	0.0230	–	–
I 50	0	50	50	0.439	0.457	0.496	0.0077	0.0169	X	C
I 88	0	87.5	12.5	0.293	0.308	0.347	0.0061	0.0197	–	–
I 100	0	100	0	0.260	0.279	0.303	0.0053	0.0190	–	–
MI 25	12.5	12.5	75	0.659	0.699	0.732	0.0088	0.0125	X	B
MI 25	12.5	12.5	75	0.662	0.709	0.755	0.0113	0.0159	–	–
MI 35	17.5	17.5	65	0.500	0.543	0.534	–	–	X	B
MI 50	25	25	50	0.319	0.332	0.354	0.0047	0.0142	X	C
MI 75	37.5	37.5	25	0.200	0.203	0.215	0.0022	0.0109	Poor	–
MI 94	47	47	6	0.153	0.165	0.165	0.0023	0.0137	–	–

[a]For coefficient of friction, displacements refer to axial shortening and correspond to shear displacements of 2.32, 4.61, and 9.21 mm. The initial uncompacted gouge thickness was 1 mm in all cases. For "Thin Section" and "Texture," "–" means no thin section or textural information and "X" means that a thin section was prepared.

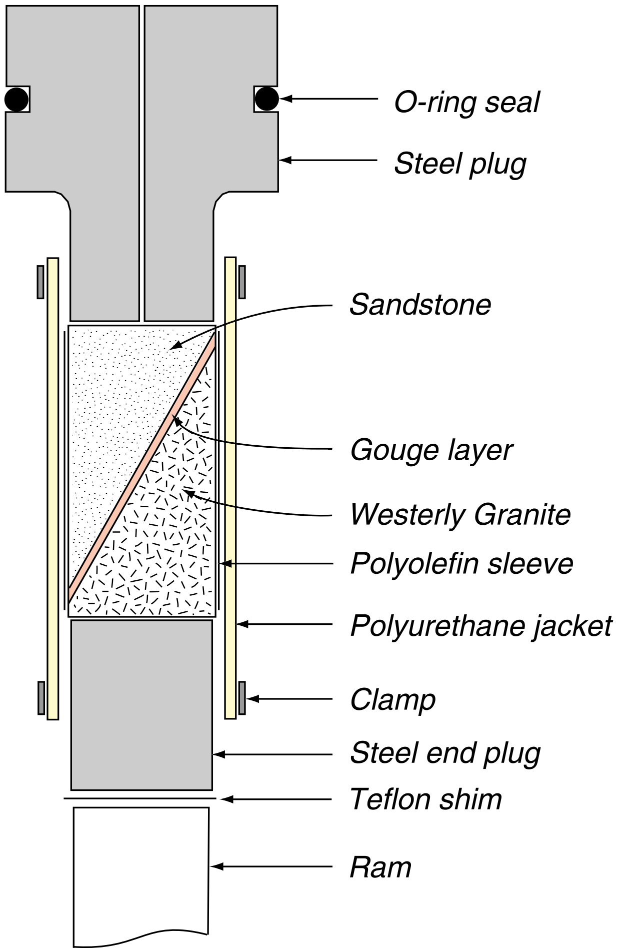

Figure 2. Experimental setup for triaxial saw cut tests.

[12] The sample assembly and pore pressure lines were evacuated for 25 min, after which deionized water was introduced as the pore fluid and the saturated sample allowed to equilibrate for at least 1 h at pore pressure $p_p = 1$ MPa and confining pressure of 41 MPa. Samples were then deformed at prescribed axial shortening rates and the resultant axial stress was recorded. An increase in axial stress results in increases in both shear and normal stress resolved on the saw cut. As axial stress changed during the experiment, confining pressure was adjusted once per second under computer control to maintain a constant normal stress of $\sigma_n =$ 41 MPa. Pore pressure was held constant at $p_p = 1$ MPa, and each sample was shortened up to 8 mm of axial displacement (corresponding to 9.2 mm resolved on the inclined saw cut). In each experiment, a servo-controlled axial displacement rate of 1.0 μm/s was initially applied until an axial displacement of 5.0 mm was obtained. The displacement rate was then decreased to 0.1 μm/s until a displacement of 6.0 mm, at which point it was increased back to 1.0 μm/s. The axial load was measured with an internal load cell with a precision of 0.02 MPa. The normal stress (computed on-the-fly from confining pressure and axial load) and pore pressure were computer controlled to within ±0.05 MPa. The mechanical data were corrected for the elastic deformation of the loading system, jacket strength, and reduction in contact area between the sliding blocks during deformation, ideally producing an uncertainty of less than 0.1 MPa in shear and normal tractions. A more detailed description of the stress corrections is provided in Appendix A. The accuracy of coefficient of friction determinations is estimated to be ±0.02. However, since care was taken to run all test under identical conditions, relative differences between friction values have an estimated uncertainty of ±0.01. See, for example, repeat experiments at 25% clay content in Figure 4c.

2.3. Petrographic Observations

[13] Eleven sheared samples were impregnated with epoxy and then sawed along a plane parallel to the axial direction and perpendicular to the saw cut plane to prepare thin sections for standard petrographic analysis. Two of these thin sections were of relatively poor quality (Table 1). Detailed optical microscopy was performed on the other nine thin sections using a Nikon petrographic microscope under polarized light. For each thin section, up to 37 images acquired at a magnification of 100× would be incorporated into a single mosaic (75 mm^2 in area) to map out shear localization features within the gouge layer.

3. Frictional Strength and Sliding Behavior of Gouge Mixtures

3.1. Frictional Sliding Behavior

[14] Our data for binary mixtures of montmorillonite/quartz and illite/quartz are presented in Figures 3a and 3b, respectively. For reference our data for the pure end-members of quartz, montmorillonite and illite are also included in Figures 3a and 3b. The ternary mixture data are presented in Figure 3c. The frictional strength data are normalized and presented in terms of the coefficient of friction $\mu = \tau/(\sigma_n - p_p)$, where τ is the shear stress resolved on the saw cut surface.

[15] Several common features were observed in the frictional sliding data. First, only stable sliding behavior occurred. Second, the frictional strength of a sample would initially rise quickly and achieve a relatively constant value after 1–2 mm slip. At this point, strength typically reverted to an approximately linear strain hardening response. For each sample, the frictional coefficient values attained at axial displacements of 2.00, 4.00, and 7.98 mm (corresponding to shear displacements of 2.32, 4.61, and 9.21 mm resolved on the saw cut) are compiled in Table 1. Third, in all three types of mixture the frictional strengths fall between the end-members comprised of pure quartz (maximum strength) and pure clay (minimum strength). Furthermore, frictional strength decreases monotonically with increasing clay content. Fourth, as described in section 3.3, velocity neutral to strengthening response was observed in all samples. That is, increased slip rate resulted in no change or increased shear strength during each test. In response to the step change in displacement rate, a relatively small change in friction coefficient was observed in all the samples, except MI35 (Figure 3c, 5 mm displacement) which showed an anomalously large irreversible strength drop when the displacement rate was lowered by an order of magnitude.

3.2. Coefficient of Friction as a Function of Clay Content

[16] Our data on the friction coefficient values at the three axial displacements of 2.00, 4.00, and 7.98 mm (Table 1)

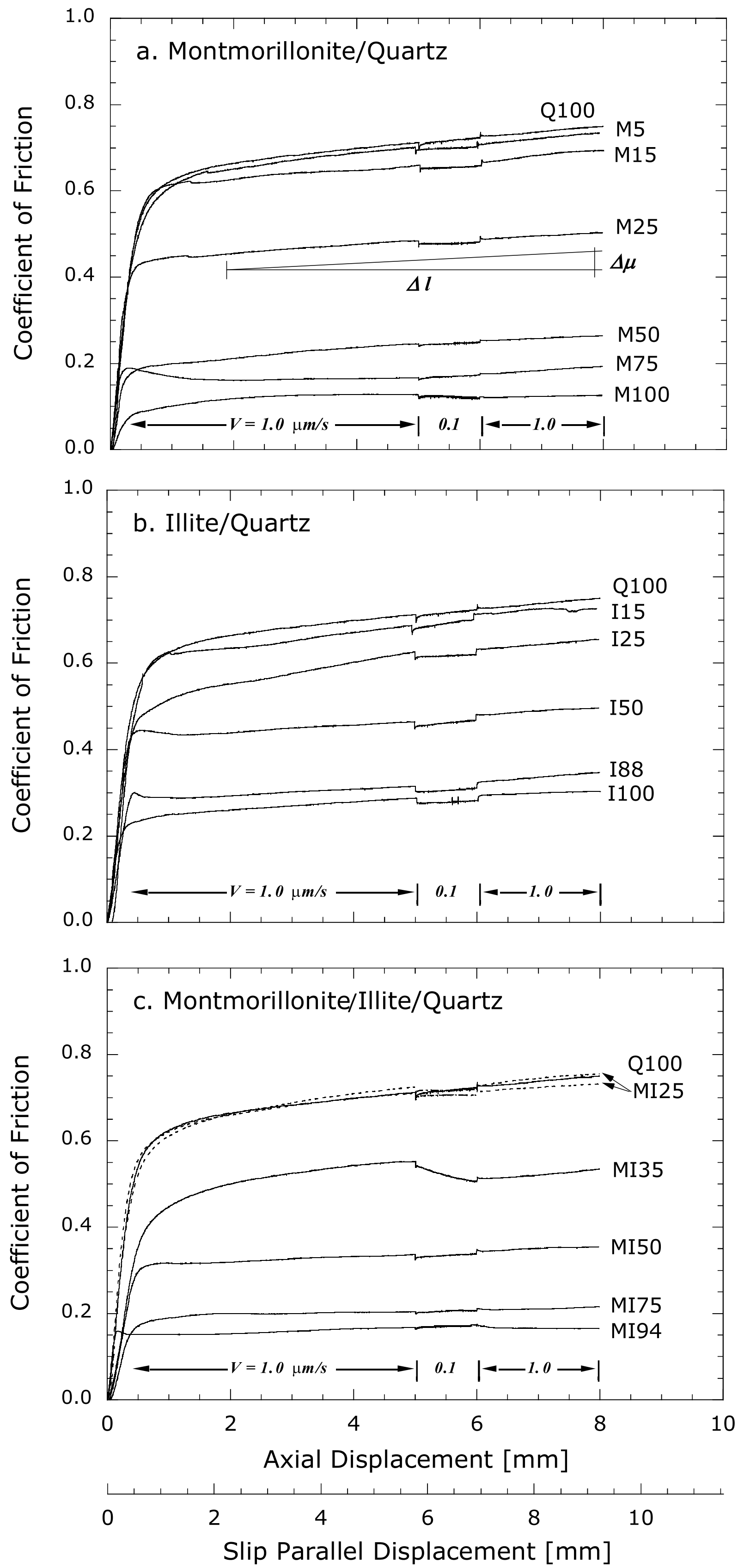

Figure 3. Friction coefficient as a function of axial displacement for (a) montmorillonite/quartz, (b) illite/quartz, and (c) montmorillonite/illite/quartz mixtures. To estimate strain hardening of the gouge due to slip, a slope for the data between 2.00 and 7.98 was calculated.

show that strain hardening could increase the frictional coefficient by up to 13% with displacement over this range. To analyze the influence of clay content on frictional strength, we compare the friction coefficient values measured at the same axial displacement of 7.98 mm, near the end of each experiment (Figure 4). In general, uncertainty in the coefficient of friction due to measurement error and reproducibility in our experiments is typically ±0.01 (less than the symbol size) for comparison of results between tests. We estimate that absolute accuracy, for comparing results to other published data that might use different test geometries is approximately ±0.02. We also use horizontal error bars for our illite samples to indicate the uncertainty in composition due to the quartz impurities present in the illitic shale that we used as a test material.

[17] As shown in Figure 3, the friction coefficient as a function of axial displacement (between 2.00 and 7.98 mm) is approximately linear, and there seems to be an overall trend for the hardening rate to increase with decreasing clay content. A linear fit to the mechanical data provides an estimate of $\Delta\mu/\Delta l$, the ratio between changes in friction coefficient and axial displacement. Since the hardening rate is conventionally defined by the ratio between changes in strength and shear strain, we will analogously characterize the hardening rate associated with frictional sliding by the ratio $h = \Delta\mu/(\Delta s/t)$, where Δs denotes the shear slip on the saw cut ($=1.156\Delta l$ in our experimental configuration) and t the thickness of the gouge layer (=1 mm nominally). The hardening rates so evaluated are compiled in Table 1. Two samples (MI35 and M100) were not included in this calculation. As noted earlier, the behavior of the ternary mixture MI35 is somewhat anomalous. As for the pure montmorillonite sample (M100), its slope is almost flat, rendering it difficult to come up with a meaningful estimate of a hardening rate. Since we do not measure gouge thickness during the experiments, we can only place a lower bound on shear strain. Pure quartz gouge layers have an initial porosity of 40%–50% during sample preparation and may compact to 6%–10% during shearing. Clay samples may have initial porosity of 60% and undergo significant volume loss during shearing. Thus layer thickness during shearing is probably in the 0.2–0.5 mm range and will depend on clay content. Gouge thinning under these normal stress conditions has been measured more precisely, for example, by *Ikari et al.* [2009].

[18] As shown in Table 1, the high clay content samples all have the lowest strain hardening rates. The end-member clay samples (M100, I100, and MI94) all show essentially zero hardening slopes by 8 mm displacement (Figure 3). Microstructural observations discussed in section 4 indicate significant quartz grain comminution in the high quartz content samples. We interpret the sustained strain hardening shown in Figure 3 as resulting from continued grain crushing and evolution of the fault gouge. This process and the accompanying evolution of frictional properties were documented, for example, by *Biegel et al.* [1989]. The strain hardening trends are not likely to be an artifact of the test geometry since identical procedures were used in experiments that show hardening and in experiments that have no hardening.

[19] Most previous studies have focused on the frictional sliding behavior of a binary mixture of montmorillonite/quartz. For comparison, we compile in Figure 4a published data acquired under both high-stress (closed symbols) and low-stress (open symbols) conditions. Our results (solid squares) are qualitatively similar to the previously published data in that the frictional strength degradation with increasing clay content can be characterized by the three regimes postulated by *Lupini et al.* [1981]. In regime 1 (test compositions of Q100, M5, and M15), the strength reduction in friction coefficient as the clay content increased to 15% was so small that the strengths of the three samples were comparable to that predicted by Byerlee's rule. In regime 2 (M15, M25, M50, M 75) a rapid drop in friction coefficient from 0.679 to 0.193 was observed in four samples with clay content ranging from 15% to 75%. In regime 3 (M75, M100), the strength reduction was stabilized with a modest decrease of friction coefficient to attain the minimum value of 0.126 for the 100% montmorillonite gouge. In a recent study, *Ikari et al.* [2007] also measured the effect of clay content on frictional strength, although their samples were partially saturated and therefore did not control pore pressure. Nevertheless, their highest water content samples show a very similar trend to the data plotted in Figure 4a.

[20] We present the data for the illite/quartz mixture in Figure 4b. As expected, the friction coefficient of the illite end-member was higher than montmorillonite, and accordingly, the reduction in friction coefficient of this binary mixture was not as pronounced as the reduction in the montmorillonite/quartz mixture. The friction coefficient shows an approximately linear decrease with increasing clay content, clearly in discrepancy with the three regime model. Our value of 0.303 is appreciably lower that the friction coefficient of about 0.4 determined by *Morrow et al.* [1992] on illite gouge extracted from disaggregated shale using the "crush and sieve" method. It is likely that by extracting the very fine size fraction through gravity settling in a water column we managed to attain an illite separate that was more pure.

[21] We present in Figure 4c the data for the ternary mixtures. For the clay end-member of mixed illite/montmorillonite we measured a friction coefficient of 0.165, which falls between the strengths of pure montmorillonite and pure illite. For the ternary mixture, three regimes of frictional strength degradation can be recognized. In the transitional regime 2 (MI25, MI35, MI50, and MI75), a rapid decrease of friction coefficient from 0.756 to 0.215 was observed as the clay content increased from 25% to 75%. Shear strength based on a simple linear-weighted average of end-member strengths would plot as a straight line in Figure 4c and does not capture the detailed variations in friction. An improved fit to the data, plotted as the dashed line in Figure 4c, is generated by averaging the trend lines for montmorillonite/quartz and illite/quartz binary mixtures. Since the data in Figure 4c come from equal fractions of montmorillonite and illite mixed with quartz, a simple averaging of the montmorillonite/quartz strength and illite/quartz strength at each clay concentration should provide a reasonable approximation to the ternary mixture strength. While the general sigmoidal shape reflects the dominant trends in the observations, this calculation under-predicts the friction coefficient in regime 1 and over predicts it in regime 3. To our knowledge, there have not been any other such measurements on a ternary mixture under high stress. *Tiwari et al.* [2005] recently reported ring-shear measurements on a ternary mixture of kaolinite, quartz and feldspar, and smectite. However, since their low-stress data are not in a

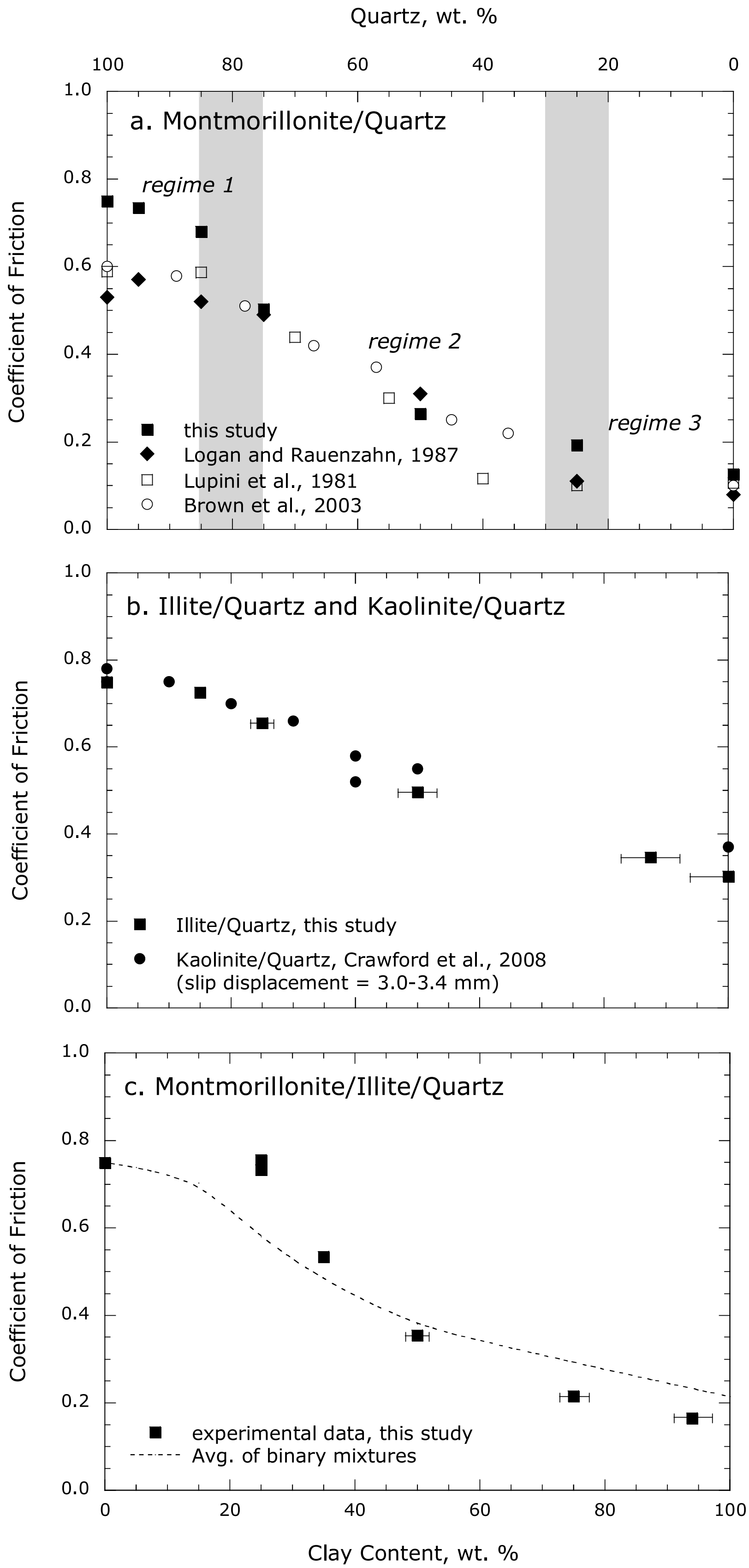

Figure 4. Friction coefficient of the runs shown in Figure 3 after 7.98 mm of axial displacement for (a) montmorillonite/quartz, (b) illite/quartz, and (c) montmorillonite/illite/quartz. For comparison, data from previous studies on sand-clay mixtures.

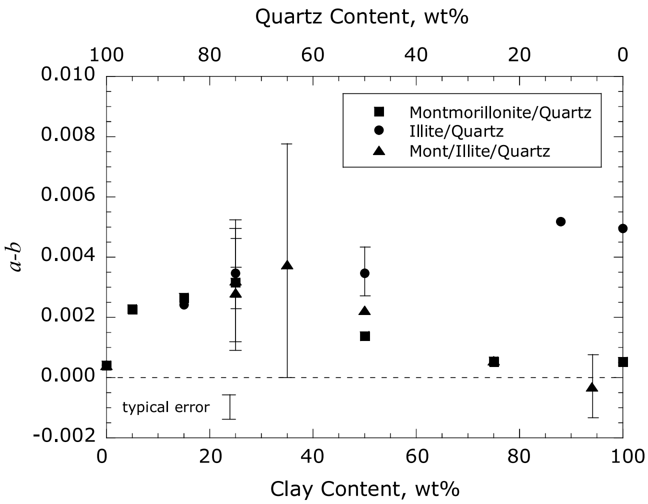

Figure 5. Velocity dependence of frictional sliding in clay mixtures where positive $a - b$ values indicate velocity strengthening and negative values indicate velocity weakening.

form that can be conveniently compared to ours, they are not included here.

[22] We have chosen to present the data in terms of the better constrained dry weight fraction. It should be noted that soil mechanics studies typically report data in terms of the volumetric clay fraction, which can be determined only if grain densities of all the minerals can be specified. Nevertheless, we expect plotting the data as a function of volume fraction would produce similar trends in strength. Since the dry solid grain density of illite (2680 kg m^{-3}) is nearly equivalent to that of quartz (2640 kg m^{-3}), the volumetric fraction plot for the illite/quartz mixture would be almost identical to the gravimetric fraction plot in Figure 4b. However, since the density of montmorillonite is more variable with addition of interlayer water, its value may be as low as 2000 kg m^{-3}, which would result in a volumetric clay content that is greater than the weight percent, corresponding to an increase in absolute value by up to 7% and 4% in the binary and ternary montmorillonite mixtures, respectively. The frictional strength data plotted as a function of volumetric clay content would appear to be shifted slightly to the right, thus enhancing the curvature in Figures 4a and 4c.

3.3. Velocity Dependence of Frictional Sliding

[23] The velocity dependence of steady-state frictional sliding can be characterized by the quantity $d\mu_{ss}/d\ln V$, were μ_{ss} denotes the steady-state coefficient of friction at a slip velocity V. In the context of the rate- and state-dependent friction model [*Dieterich*, 1979], this quantity is given by the difference $a - b$, with a and b characterizing the "direct" and "evolution" effects in response to perturbations in slip velocity, respectively [*Paterson and Wong*, 2005]. Positive and negative values of $a - b = d\mu_{ss}/d\ln V$ thus correspond to velocity strengthening and weakening, respectively.

[24] Since in each experiment we made two-step changes in the loading velocity (Figure 3), the velocity dependence can be inferred from the corresponding changes in friction coefficient. Data have been detrended to remove the long-term strain hardening before determining rate dependence. We present in Figure 5 our data for the velocity dependence of the friction coefficient as a function of clay content for the three types of mixture. The uncertainty in these estimates is typically around ±0.0004, but in certain mixtures (such as MI35 which showed an anomalously large strength drop in response to the velocity perturbation) uncertainties in estimating steady-state friction and consequently $a - b$ were larger, as indicated in the plot. Our data for $a - b$ of all three types of gouge mixtures range from near-zero to slightly positive, in basic agreement with previous observations of *Logan and Rauenzahn* [1987], *Morrow et al.* [1992], *Kopf and Brown* [2003], and *Ikari et al.* [2007, 2009] of velocity strengthening behavior in binary mixtures of montmorillonite/quartz and illite/quartz.

[25] In the illite/quartz mixture, there is an overall trend for $a - b$ to increase with increasing clay content (Figure 5). Since the friction coefficient of this binary mixture decreases linearly with clay fraction (Figure 4b), this results in a negative correlation between frictional strength and velocity strengthening (Table 1). In comparison, the velocity dependence of the other two mixtures is more complicated, with qualitatively different behaviors in the three regimes associated with strength degradation. In regime 1, $a - b$ increases from almost zero for pure quartz to about 0.003 for the 25% clay mixtures of montmorillonite/quartz and montmorillonite/illite/quartz. This is followed by a decrease of $a - b$ in regime 2, ultimately approaching almost neutral rate dependence in regime 3 for the montmorillonite and montmorillonite/illite end-members. It is noteworthy that the rate dependence in the ternary system essentially follows the rate dependence of the montmorillonite/quartz binary mixtures. A possible explanation is that montmorillonite, being weaker than illite, organizes into localized slip surfaces and dominates the shearing micromechanics. This interpretation is consistent with the observed dominance that montmorillonite has relative to illite in controlling frictional strength in the ternary mixtures (right half of Figure 4c).

4. Microstructural Observations

4.1. Description of Gouge Textures

[26] We observed a number of textural features in the sheared gouge mixtures, including Riedel shear bands, boundary shears, and clay mineral fabric which may become more or less pronounced as the gouge composition varies. To describe the texture and fabric of these gouges, we will follow the notation shown in Figure 6 which is based on the classification scheme of *Logan et al.* [1979]. All micrographs in this paper are presented with top-to-the-left sense of shear.

[27] The gouge textures in our sheared montmorillonite/quartz mixtures are similar to those documented by *Logan and Rauenzahn* [1987], even though the gouge mixtures in this previous study involved somewhat more complicated loading paths. In regime 1, the montmorillonite grains are typically entrapped in the void space of the quartz particles and the gouges seem to have undergone significant shear compaction before shear localization would occur. Many of the quartz grains have been intensely comminuted with shear localization developed along R-, Y-, and boundary shears. Although they share many common features, the Riedel

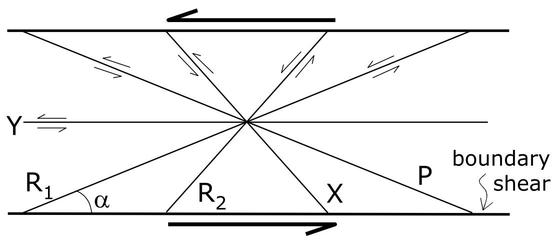

Figure 6. Classification of shear localization developed in deformed gouge layers [after *Logan et al.*, 1992].

shears in our samples are not as dense as those documented by *Gu and Wong* [1994] in an ultrafine quartz gouge. Two micrographs from the samples M5 and M15 are shown in Figure 7. The gouge layer in M5 shows an asymmetric distribution of large quartz grains with typical grain size of about 100 μm and aggregates in the upper part of the gouge and comminuted grains in the lower half. Short Riedel shears are present in each half but have been crosscut by the Y-shear. In this sample, strain concentrates along Y-shears, which separate coarser particles from a finer matrix. It may be that most of the sliding is initially accommodated at the interface of the country rock and gouge, thus developing a thick boundary shear of finer material. Textures from this regime are diagrammatically represented as *texture A* in Figure 7.

[28] In regime 2, the quartz grains in the gouge mixture have a tendency to congregate in the middle of the gouge layer, away from the boundaries and often surrounded by R-shears. In comparison to samples sheared in regime 1, the quartz grains show appreciably less comminution or microcracking. At higher magnification, there is a noticeable particle size gradation near the R- and boundary shears with finer quartz and clay particles entrained in the shear and larger, less deformed grains further away. A clay foliation in the P-orientation is often observed to develop at 155°–160° to the shear direction in these samples. In most samples, several continuous R-shears could be observed, indicating that they might have been active toward the end of the experiment. Many of the samples contain Y- and P-shear bands that link discontinuous Riedel shears. We classify these microstructures as belonging to *texture B*. As indicated by the arrows in sample M50 (Figure 7), many of the quartz grains are relatively intact with little cracking and they are surrounded by the clay particles. The clay has also migrated to the country rock-gouge interface to form a thin boundary shear, with very few Y-shears present. We had very limited observations on montmorillonite samples from regime 3, but *Logan and Rauenzahn* [1987] reported "discontinuous alignment of grains" and "little fracturing of quartz" in a sample with 75% montmorillonite. They also observed "pervasive alignment of clay grains" in the R_1 and Y orientations. This microstructural development is categorized as *texture C* in Figure 7.

[29] Our observations on the ternary mixture point to gouge textures that are qualitatively similar to those of montmorillonite/quartz. This is illustrated by micrographs of MI25 and MI35 (Figure 7). We also observed *texture B* in binary mixtures with illite content equal to or greater than

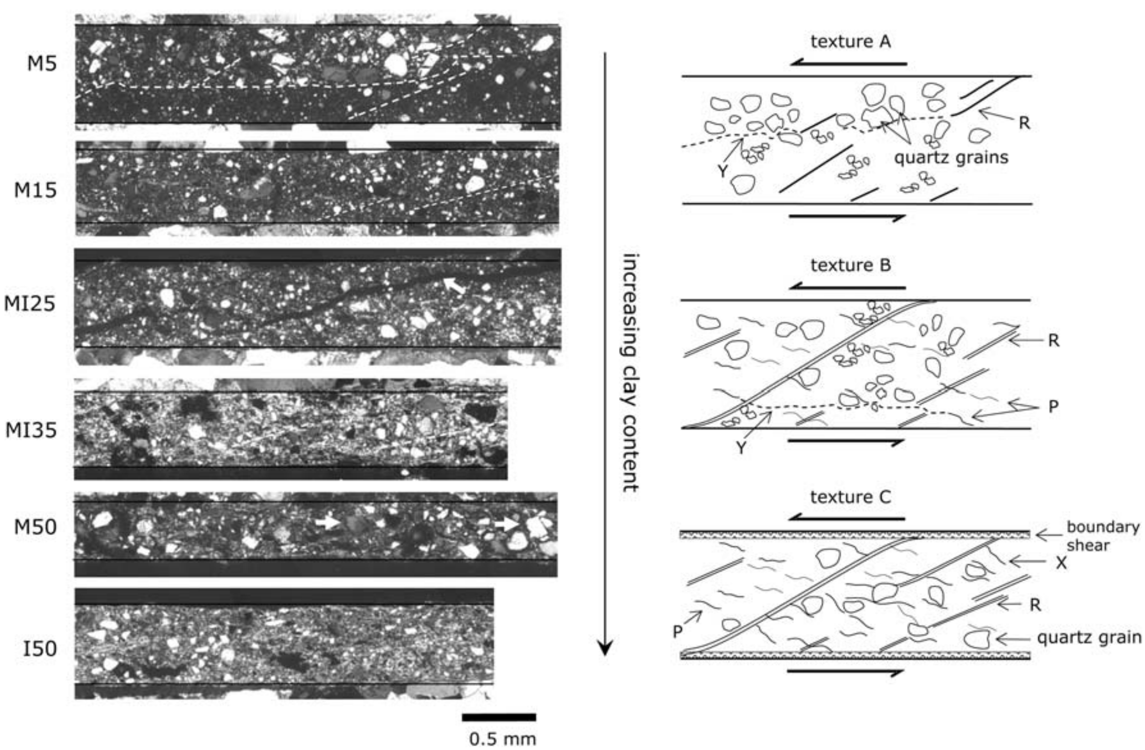

Figure 7. Micrographs of clay-quartz gouges under polarized light after 9.2 mm of fault parallel slip. Dashed lines highlight shear bands. The white arrow in MI25 points to an R-shear and in M50 the arrows point to large intact quartz grains. The micrographs have three classes of textures that vary with clay content.

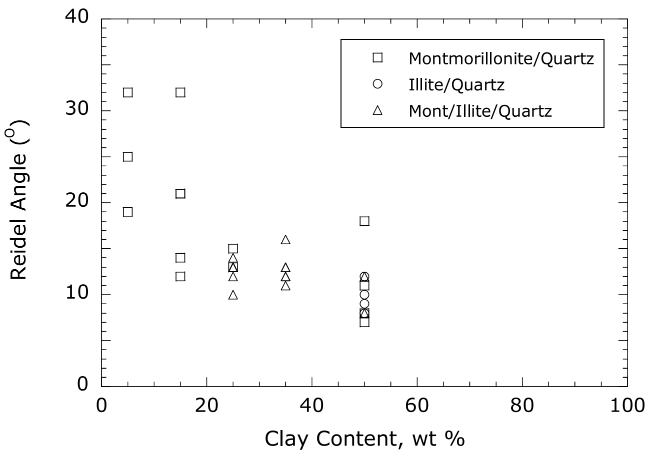

Figure 8. Reidel shear angle in gouge samples show a marked decrease in angle with increasing clay content at the transition from regime 1 to 2.

50%. A micrograph of I_{50} is presented in Figure 7. It should also be noted that deformation features documented by *Moore et al.* [1989] in sheared heated illite gouges are quite similar to *Logan and Rauenzahn*'s [1987] observations on 100% montmorillonite.

4.2. Orientation of Riedel Shear Localization

[30] Although the densities of Riedel shear in our samples are relatively low, we were able to characterize the orientation of R-shears in selected samples with clay contents between 5% and 50%. We measured the angle α of the R_1 shear with respect to the boundary between the gouge and country rock (Figure 6), and the data are plotted as a function of the clay content in Figure 8. While the samples with low clay content show greater scatter, there is an overall trend for the Riedel shear angle to decrease with increasing clay content.

[31] Such a decrease of Riedel shear angle can be attributed to reduction of the bulk strength of the gouge mixtures [*Gu and Wong*, 1994]. If the gouge can be approximated as a noncohesive material with its pressure-dependent bulk strength characterized by an angle of internal friction μ_i, then stress equilibrium at the interface of the country rock and gouge layer would constrain the limiting state of stress and principal stress orientations within the gouge layer at the onset of Riedel shear localization, which in turn determine the orientations of the Riedel shears. In particular, *Gu and Wong* [1994] derived the following expression for the orientation of the R_1-shear:

$$\alpha = \frac{\pi}{4} - \frac{1}{2}\tan^{-1}\left(\frac{\mu}{-\mu_i^2 + \left(1+\mu_i^2\right)\sqrt{1-\left(1+\mu^2\right)/\left(1+\mu_i^2\right)}}\right) + \frac{\tan^{-1}\mu_i}{2}. \tag{1}$$

We plot in Figure 9 this theoretical prediction of the Riedel shear angle as a function of the friction coefficient μ (corresponding to the ratio between the shear and normal stresses resolved at the rock-gouge interface) for fixed values of the internal friction coefficient μ_i. For comparison, we plot our gouge mixture data on the mean value of the angle α as a function of friction coefficient μ. Data for the ternary and montmorillonite/quartz mixtures considered to be in regimes 1 and 2 are shown in open and dark symbols, respectively. A data point for a binary mixture made up of 50% illite is shown. We also include the data of *Gu and Wong* [1994] for a highly sheared coarse quartz gouge (sample WGQP17) and of *Moore et al.* [1989] for heated Fithian shale (made up of 80% illite). Comparison of the laboratory data with theoretical prediction suggests that the transition from regime 1 to 2 in the ternary and montmorillonite/quartz mixtures is associated with a decrease in the bulk strength of the gouge mixtures, corresponding to a reduction of the internal friction coefficient from above 0.8 to less than 0.6. A binary mixture with relatively high illite content is predicted to also have an internal friction coefficient of <0.6.

[32] A limitation of this mechanical interpretation should be noted. The equilibrium condition and therefore equation (1) should strictly apply only in the vicinity of the rock-gouge interface with the implicit assumption that shear localization develops along planar features, whereas the Riedel shears are often curvilinear and the angle measurements typically made near the midsection of the gouge layer.

5. Discussion

[33] *Skempton* [1964] postulated a general correlation between saturated residual friction of a soil, and its clay content that seems independent of clay mineralogy. *Lupini et al.* [1981] emphasized that the degradation of frictional strength with increasing clay content is nonlinear, typically

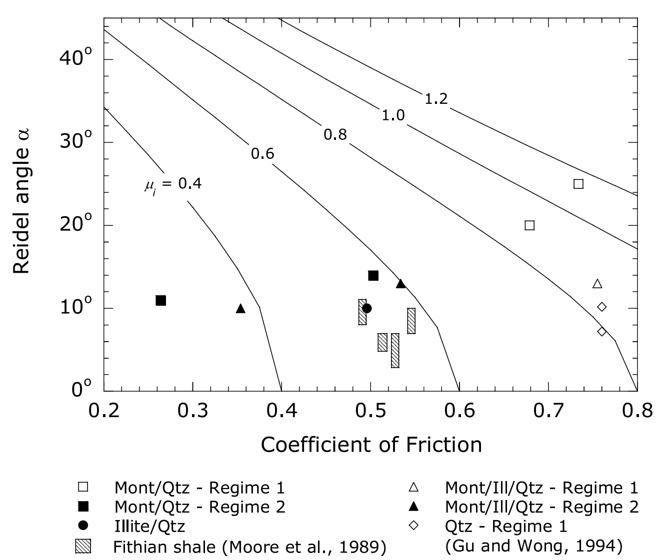

Figure 9. Reidel shear angle as a function of the friction coefficient. The solid curves are theoretical predictions of the Reidel shear angle as a function of the friction coefficient for fixed values of the internal friction coefficient μ_i from equation (1). The points represent the average Reidel angle from experimental data for our mixtures shown Figure 8, from *Gu and Wong* [1994] for coarse quartz, and from *Moore et al.* [1989] for illite-bearing Fithian shale. Open and closed symbols represent samples belonging to regimes 1 and 2, respectively.

falling on a sigmoidal curve that can be separated into three distinct regimes. In this study, we conducted frictional sliding experiments on saturated mixtures at an effective normal stress of 40 MPa. Our data for the influence of clay content on frictional strength show that while the montmorillonite/quartz mixture and montmorillonite/illite/quartz ternary mixture follow a sigmoidal trend analogous to that observed in soil mechanics at relatively low normal stresses, the illite/quartz mixture is fundamentally different in that its strength degradation follows an approximately linear trend with increasing clay fraction.

[34] Our microstructural observations particularly in the montmorillonite/quartz mixtures have identified certain shear localization fabrics that are characteristic of three regimes of frictional strength degradation. Since sand grains may be larger than clay particles by several order of magnitude, in a sandy mixture with low clay content (such as our gouge mixtures in regime 1), the clay minerals would tend to collect in the voids of the larger framework quartz grains and accordingly the applied stresses are primarily accommodated by force network chains that connect the contacting quartz grains. Since the stresses involved here are higher than those in soil mechanics tests, the contacting grains may undergo significant microcracking and comminution. As the clay content increases to beyond a critical fraction, the voids are completely occupied by the clays, inducing the quartz grains to disperse within an interconnected clay matrix. This allows the possibility of development of clay foliation as a gouge failure mode, and as clay content increases this shear localization mechanism evolves to become dominant in regime 2. Because of the significant contrast in frictional strength between the clay and quartz, the overall friction coefficient would undergo significant reduction with this development. Since quartz particles are embedded in the clay matrix, they act as high-strength "barriers" for the development of thoroughgoing Riedel shears within the clay even though the matrix is interconnected. As the clay content further increases, it becomes less likely for the quartz barriers to impede the development of shear localization within the clay matrix, and ultimately in regime 3 the quartz barriers play such a minor role that the failure mode is predominately due to Riedel shear localization in the clay. As a result, the friction coefficient in regime 3 is comparable to that in a pure clay gouge.

[35] *Lupini et al.* [1981] referred to these three regimes of strength degradation as "turbulent shear," "transitional," and "sliding shear." In this study, we have avoided the use of this somewhat misleading terminology. The term "turbulent shear" may imply the absence of any patterning of strain such as Riedel shear localization, which is actually an important mechanism of gouge failure involving the stress-supporting quartz framework in regime 1. To associate regime 3 with "sliding shear" would suggest that this is a mechanism that applies only to clay, thus ruling out localized shear slip along Riedel bands in the quartz matrix that occurs in regime 1.

5.1. Evolution of Frictional Strength in Synthetic Gouge Mixture With Slip Distance

[36] By definition the residual strength corresponds to the steady-state strength under fully developed flow conditions, with the absence of any strain hardening. As shown in Figure 3, our predominately clay samples (with zero or small quartz content) did approach such a residual strength by a total slip of 5–6 mm. In contrast, mixtures with higher quartz contents showed appreciable hardening. Increasing quartz content generally resulted in increasing strain hardening rate (computed in Table 1) and in many cases, samples had not achieved residual strength by 8 mm axial shortening. This persistent strain hardening (which has also been documented in other high-stress studies) has important implications for the present analysis. First, the three-regime model developed by *Lupini et al.* [1981] was based on low normal stress data in which grain crushing and comminution were minimal. At high normal stress, however, grain crushing becomes important and is a primary mechanism for strain hardening [*Biegel et al.*, 1989]. In our pure quartz experiment, strength increases by 13% between 2.3 and 9.2 mm slip. Therefore, regime 1 in the *Lupini et al.* [1981] model, which is dominated by relative slip of quartz-on-quartz grain contacts, may exhibit significantly different properties at high normal stress, especially in relation to how the frictional strength evolves with strain hardening. Second, fully developed residual flow may not be achievable at high normal stress using the triaxial geometry with its inherent limitation on total slip. Accordingly, strength data during strain hardening should be compared only at similar slip distances or shear strains.

[37] We compare our data to other published data for similar mixtures deformed to different slip distances. Our data in Figure 3 correspond to frictional strengths attained at the maximum axial displacement of 8 mm (slip distance of 9.2 mm) in our experiments. To underscore the influence of hardening on the evolution of frictional strength with slip distance, we also plot in Figures 10a and 10b our data at axial displacement of 2 mm (slip distance of 2.3 mm) for the montmorillonite/quartz and illite/quartz mixtures, respectively. As noted earlier, this slip distance marks the onset of approximately linear hardening behavior in our synthetic gouges (Figure 3), which is characterized by the hardening rate h compiled in Table 1. The value of h varies by a factor of 7, ranging from 0.002 to 0.015. For the same type of mixture, there is an overall trend for h to increase with increasing quartz content, possibly because the hardening rate of quartz (associated with cataclastic processes such as microcracking and comminution) is proportionately higher than that of clay. At the same quartz content, the hardening rate of the illite/quartz mixture is typically higher than the other two mixtures, implying a positive correlation between h and μ. Indeed, normalizing the hardening rate by the friction coefficient (at an intermediate axial displacement of 4.0 mm) shows that the ratio h/μ falls in a relatively narrow range of 0.011–0.030 (Table 1). While it is implausible that the strain hardening can persist to infinite distance, our data show that the threshold slip distance at which the hardening effect would "saturate" has to be longer than the maximum distance in our experiments.

[38] For comparison, Figure 4a also includes montmorillonite/quartz mixture data for both high-stress (solid symbols) and low-stress (open symbols) conditions that were presented by *Logan and Rauenzahn* [1987], *Lupini et al.* [1981], and *Brown et al.* [2003]. *Takahashi et al.* [2007] recently presented data for a montmorillonite/quartz mixture (deformed at an effective normal stress of 75 MPa) to slip distances of about 2.2 mm, which we

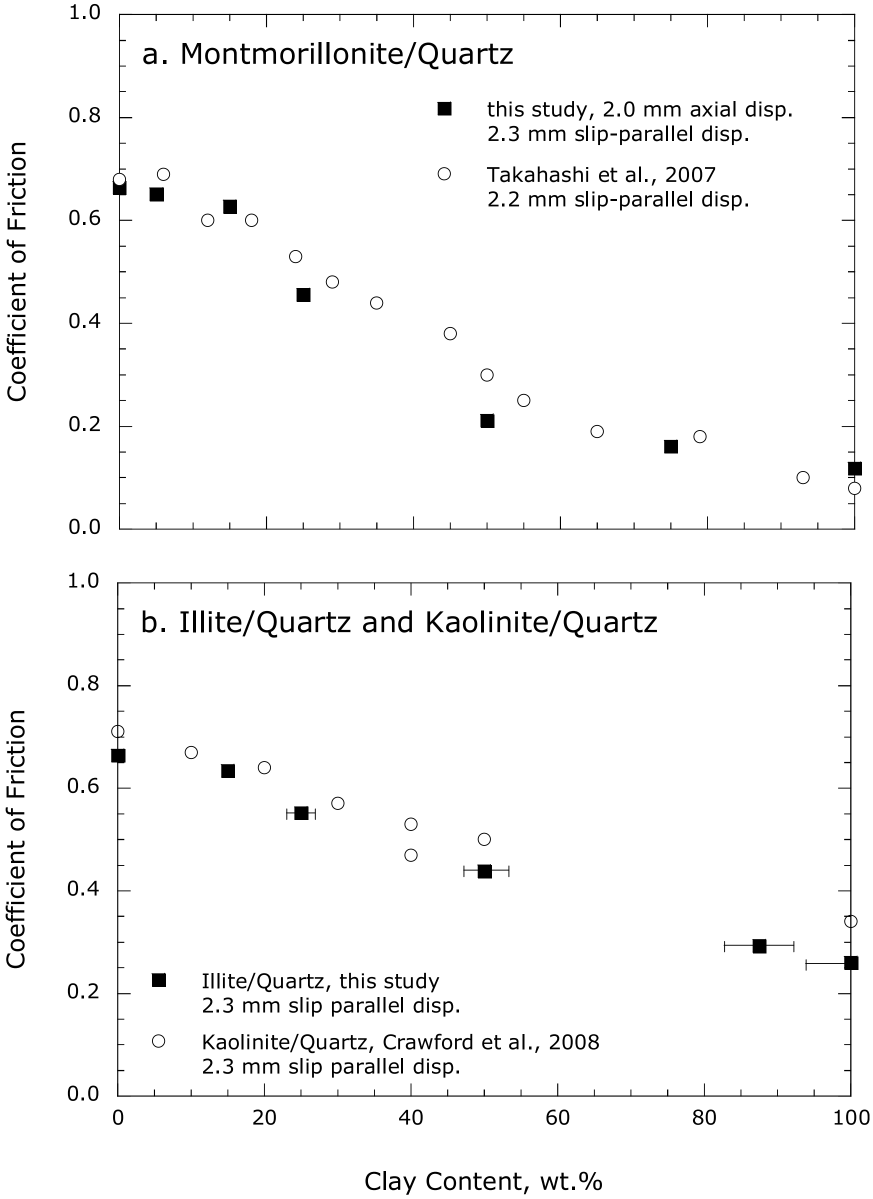

Figure 10. Coefficient of friction at lower shear strain as a function of clay content. Data obtained at the end of experimental runs (presented in Figure 4) showed that the degradation of strength can follow linear or sigmoidal trend and because of slip hardening of the gouge the trends may persist or evolve.

included in Figure 10a. *Crawford et al.* [2008] also conducted frictional sliding experiments on a binary mixture of kaolinite and quartz (at an effective pressure of 50 MPa). Their data were presented in term of friction coefficient as a function of shear strain, but Crawford has kindly furnished us with the data plotted as a function of slip distance. We show in Figures 4b and 10b, the data of *Crawford et al.* [2008] for water-saturated kaolinite/quartz data at the maximum slip distance (which ranged from 3.0 to 3.4 mm) and at 2.3 mm, respectively.

[39] The low-stress studies of *Lupini et al.* [1981] and *Brown et al.* [2003] show residual friction coefficients of montmorillonite/quartz mixtures that plateau at $\mu \sim 0.6$ in the 85%–100% quartz range. This is regime 1 as discussed by *Lupini et al.* and is expected to differ from higher normal stress data associated with significant grain crushing and strain hardening. Indeed, our high-stress data for M5 and M15 at maximum slip distances show friction coefficient significantly higher, in the range of 0.68–0.75 (Figure 4a). For similar mixtures, *Takahashi et al.* [2007] reported friction coefficients in the range of 0.6–0.7 (Figure 10a) at a relatively short slip distance of about 2.3 mm, which represent lower bounds for the strength at longer slip distances. For pure quartz at slip distance of 3.42 mm, *Crawford et al.* [2008] reported a friction coefficient of 0.78 (Figure 10b) that is comparable to our value (Figure 4a). However, there is an apparent discrepancy between these recent high-stress studies and the data of *Logan and Rauenzahn* [1987], in that the latter consistently showed much lower friction coefficients in regime 1 (Figure 4). Since *Logan and Rauenzahn*

[1987] conducted their tests to relatively high slip distances, it is unlikely that this discrepancy can be attributed to strain hardening effect. A plausible explanation is that their samples were subjected to rather complicated "preconditioning," which might have built in complex deformation fabrics in their samples before they were subsequently deformed.

[40] All studies plotted in Figure 4a give similar strength results in regime 2. In regime 3, the frictional behavior of the clay-rich mixture is dominated by montmorillonite, the strength of which (in a water-saturated state) is expected to increase with increasing normal stress [*Kopf and Brown*, 2003; *Moore and Lockner*, 2007]. The frictional strength is also sensitive to fluid chemistry. *Brown et al.* [2003] and *Kopf and Brown* [2003] used seawater (roughly equivalent to a 0.5 M NaCl solution) whereas *Logan and Rauenzahn* [1987], *Moore and Lockner* [2007], and our study used deionized water. We should also note that *Saffer and Marone* [2003] and *Ikari et al.* [2007] presented frictional data on binary sand-clay mixtures, but given the partially saturated state of their simulated gouge samples it is difficult to quantitatively compare their data with that of water-saturated gouges [*Moore and Lockner*, 2007], and so their data are not included.

[41] *Crawford et al.* [2008] measured a friction coefficient of 0.37 for pure kaolinite, somewhat higher than our value of 0.303 for illite (Table 1). As shown in Figure 4b, the data for both illite/quartz and kaolinite/quartz mixtures follow approximately linear trends that are considerably simpler than the three-regime model of *Lupini et al.* [1981]. The implication is that the *Lupini*-type nonlinear correlation commonly observed in soil mechanics cannot be generalized to a high-stress environment independent of clay mineralogy. The friction coefficient can be a linear or nonlinear function of clay content. At this point, the extrapolation of laboratory data to a seismogenic setting made up of clay-rich fault gouge would require the interpolation of systematic measurements of various synthetic gouge mixtures. One approach is to use empirical interpolation with a ternary plot that we will present in a later section.

[42] Figure 10a shows that our data for montmorillonite/quartz at the early stage of hardening are in basic agreement with those of *Takahashi et al.* [2007], who have argued that their data are better interpreted by a trilinear model, with a frictional strength that decreases with increasing clay content along two linear segments separated by a pronounced drop at a clay fraction of about 50%. While it remains moot whether the data at short slip distances are better fitted by a trilinear model rather than the three-regime model of *Lupini et al.* [1981], comparison with our data at longer slip distances (Figure 4a) shows that strain hardening significantly enhances the friction coefficients of the mixtures with higher quartz contents and as a result, the strength degradation with increasing clay content deviates significantly from the trilinear trend postulated by *Takahashi et al.* [2007].

[43] Figure 10b shows that the data for illite/quartz and kaolinite/quartz at the early stage of hardening are similar to those at longer slip distances (Figure 10c), in that the degradation of strength with increasing clay content is approximately linear. Given the approximately linear hardening behaviors, one would expect such a linear trend to persist with the progressive development of strain hardening.

[44] For our comparison, we have selected data for a given mixture with different clay contents at a fixed axial displacement (or shear slip along the saw cut surface), which would imply a fixed shear strain only if the gouge thickness is identical. While the shear strain is the more appropriate parameter for characterizing strain hardening, it cannot be determined directly in a triaxial configuration and a number of assumptions must be made to infer it from displacement data. Since our samples were initially prepared with identical gouge thickness, the subsequent thickness at a fixed shear slip would be identical only if the thickness reduction induced is the same. *Crawford et al.* [2008] inferred the reduction of gouge-layer thickness from measurement of pore volume, which was then used to convert their slip displacement data to apparent shear strain, with the assumptions that the externally measured pore volume change was solely from porosity reduction in the gouge layer and that the shear-induced gouge compaction derived solely from uniaxial thinning of the gouge layer (transverse to the slip displacement). When their kaolinite/quartz data for friction coefficient at a shear strain of 5 were plotted, *Crawford et al.* [2008] observed a nonlinear trend, in contrast to the linear trends shown in Figures 4b and 10b. It seems that the gouge thickness variation was lower in a mixture with intermediate quartz content, which resulted in friction coefficients of the mixtures with 50% and 60% quartz lower than those predicted by a linear trend, and accordingly *Crawford et al.* [2008] concluded that the influence of clay content on strength degradation can be better represented by a three-regime model. It is unclear what may have caused this somewhat anomalous compaction behavior in these two samples and whether this apparently nonlinear trend would persist to longer slip and larger strain. For reference, it should be noted that our data shown in Figure 4b involve samples sheared to an apparent strain of >9.

5.2. Frictional Strength Degradation in Synthetic Gouge Mixture: Grain Packing, Cataclasis, and Strain Localization

[45] While the model of *Lupini et al.* [1981] focuses on the interplay of grain packing and strain localization (primarily in the clay matrix), our friction and microstructural data underscore the necessity of incorporating the hardening effect, particularly that related to microcracking and grain crushing in the clastic particles. We present in Figure 11a conceptual model of the interplay of grain packing, cataclasis, and strain localization in controlling the degradation of frictional strength with increasing clay content in a gouge mixture. Since some aspects of the model of *Lupini et al.* [1981] were not explicitly presented and have sometimes been misconstrued, it is useful for our discussion to include a more precise summary of this model, which can be found in Appendices B and C.

[46] *Lupini et al.* [1981] postulated that the transition from their regime 1 to 2 is associated with a qualitative change in the grain packing, from a mixture with an interconnected framework of quartz grains supporting the applied stresses to one with an interconnected clay matrix. According to this ideal packing model, the quartz grains are first assembled to form an interconnected, stress-supporting framework that has an interstitial void space with porosity ϕ_s. The clay particles are then randomly added into the void space without

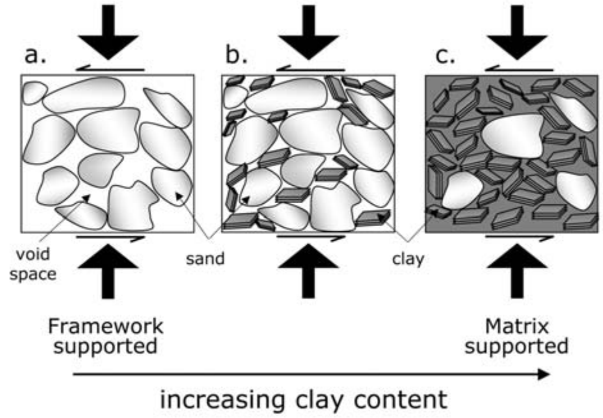

Figure 11. (a) A stress-supporting framework of quartz sand grains. (b) The clay minerals collect in the void space of the coordinated grains, and the load is accommodated by the quartz force chains. (c) As the clay fraction increases the force chains are comprised of the weak minerals that yield easily to applied stress until finally the clay content exceeds the void volume and shear strength is reduced.

disturbing the pre-existing quartz framework. As the clay content increases, a point will be reached when all the interstitial space has been filled, and further addition of clay particles necessitates the separation of quartz grains and reduction in grain contacts. The result is enhanced connectivity among the clay grains and development of an interconnected clay matrix at the inception of regime 2.

[47] In Appendix B, we show that the gravimetric clay fraction at this grain packing transition is given by

$$w_{\mathrm{cr}} = \frac{(1-\phi_{\mathrm{cl}})}{(1-\phi_{\mathrm{cl}}\phi_{\mathrm{s}})}\phi_{\mathrm{s}}, \tag{2}$$

where ϕ_{cl} denotes the porosity of the dry clay grains. According to this ideal packing model, the critical gravimetric clay fraction at the transition from regime 1 to 2 depends only on the initial quartz packing (characterized by ϕ_{s}) and clay porosity (characterized by ϕ_{cl}). An increase in pressure or normal stress will decrease both ϕ_{s} and ϕ_{cl}, but since the decrease in clay porosity is typically more pronounced than the quartz porosity, one expects the critical gravimetric fraction w_{cr} to slightly increase with increasing pressure or normal stress.

[48] While clay is highly porous at ambient conditions, its porosity may collapse resulting in significant porosity reduction under pressure. However, there is a paucity of data on clay porosity at high pressure. Some of the best data are for saturated kaolinite obtained by *Marion et al.* [1992], who reported a drastic reduction of porosity from an initial value of 62%–24% at an effective pressure of 40 MPa. Guided by their data, if we assume that in our gouge mixtures the clay porosity $\phi_{\mathrm{cl}} = 0.24$, then our montmorillonite/quartz data which indicate a critical weight fraction of about 20% (an intermediate value between 15% and 25%) would imply that the stress-bearing quartz framework had a porosity of $\phi_{\mathrm{s}} \approx 25\%$. For comparison, *Marion et al.* [1992] determined a porosity value of 33% and *Zoback and Byerlee* [1976] reported values of 22% and 23% for hydrostatically stressed Ottawa sand at an effective pressure of 40 MPa. Even though our quartz gouges were more angular than Ottawa sand and likely to be more porous than Ottawa sand under ambient conditions, our microstructural observations also indicate pervasive shear-enhanced compaction associated with comminution and microcracking in quartz that might significantly reduce the porosity of the quartz framework.

[49] If we were to consider the mixed clay (of illite and montmorillonite) as one single component in a binary mixture, then according to Figure 3c our ternary mixture data which indicate a critical weight fraction of about 30% (an intermediate value between 25% and 35%) would imply a very low clay porosity of <10%. The ideal packing model of a binary mixture may be of limited applicability in this context, and indeed the analysis can be extended to a ternary system [*Cumberland and Crawford*, 1987], but given the paucity of constraints on the additional parameters, the use of a more involved analysis is unlikely to provide insights into our ternary mixtures data.

[50] For a binary mixture at the critical condition (2), the ideal packing model predicts a minimum in porosity and a maximum in the P-velocity as functions of clay content at a fixed effective pressure [*Marion et al.*, 1992; *Revil et al.*, 2002; *Crawford et al.*, 2008], and this represents the only transition of importance for a sand-clay mixture under hydrostatic loading. Under shear loading and in the absence of appreciable hardening, this transition is manifested by an accelerated decrease of frictional strength at a clay fraction of 25% or so, corresponding to that observed in the montmorillonite/quartz and ternary mixtures (Figures 4a and 4c) and possibly in the kaolinite/quartz mixtures at low-shear strain as observed by *Crawford et al.* [2008]. Under stresses significantly higher than those in typical soil mechanics tests, the clastic particles may undergo pervasive microcracking and grain crushing, which are likely to enhance the friction strength with cumulative slip. This hardening effect is more pronounced in a mixture with relatively low clay content, where the clastic particles provide the stress-supporting framework. The decrease in frictional strength due to the grain-packing transition is modulated by the differential hardening rate, and the cooperative effect may result in a quasi-linear decrease of frictional strength with increasing clay content in regime 1.

[51] Under nonhydrostatic loading *Lupini et al.* [1981] postulated that there is an additional transition from regime 2 to 3 related to Riedel shear localization in the interconnected clay matrix that can develop when the quartz particles are sufficiently disperse at a relatively high clay fraction. To analyze this second transition, we will expand on their proposal that the inception of regime 3 hinges on the attainment of a critical thickness for the clay layer that separates two neighboring layers of sand grains.

[52] In Appendix C, we consider two configurations. We will consider monodisperse spheres (with diameter d and radius $r = d/2$) in a hexagonal close-packed (HCP) assemblage and a simple cubic (SC) packing which is relatively loose. Each spherical grain is covered by a concentric clay layer of uniform thickness δ (Figure 12). *Lupini et al.* [1981] proposed using the ratio $\delta/d = \delta/(2r)$ as the geometric parameter that controls the transition from regime 2 to 3. From soil mechanics data, they suggested a critical ratio of 0.1–0.4 for this transition to occur. We plot in Figure 13 the normalized clay layer thickness δ/d as a function of w_{c} for

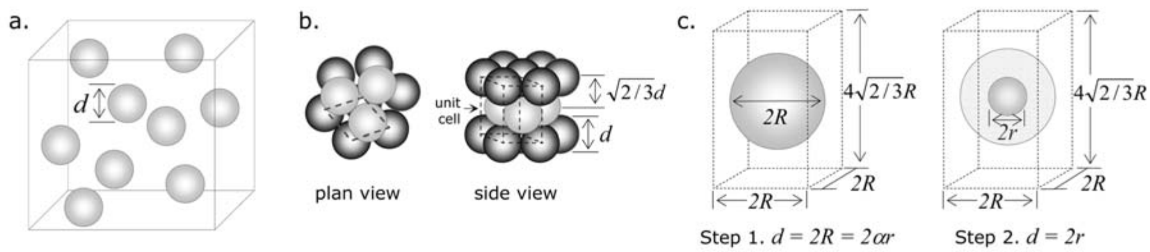

Figure 12. (a) A system of randomly dispersed spherical particles. (b) HCP particle configuration considered in our ideal packing scenario. (c) A representative HCP unit cell volume containing a spherical grain embedded within a clay matrix. The system dilates by a factor α in step 1. In step 2, the solid grain contracts to its original size within the transformed cell and the residual space is filled with clay.

these two packing arrangements, again taking ϕ_{cl} = 0.24. According to this model, our observations of a critical weight fraction of about 70% in the montmorillonite/quartz and ternary mixtures imply a normalized clay layer thickness δ/d = 0.18 and 0.30 for the HCP and SC configurations, respectively.

[53] Since we have assumed a homogeneous distribution of clay, our analytic estimates are probably less than the thickness of clay along which continuous Riedel shears may develop, in light of our microstructural observations that the spatial distribution of quartz grains can be quite heterogeneous in the sheared gouge mixtures. Our model idealizes the quartz grains as monodisperse spheres, and it is plausible that thicker clay layers can readily develop in a less sorted system made up of angular grains. Cataclasis and grain size reduction of the sand would produce a highly heterogeneous particle size distribution with an overall shift toward the clay-size fraction. All these processes may contribute to hardening, which can dampen the strength decrease as predicted by the idealized model of monodisperse spheres embedded in an interconnected matrix.

[54] The interplay of grain packing, cataclasis, and strain localization associated with the two transitions is manifested by significant drops of frictional strength which map out three regimes of strength degradation in the montmorillonite/quartz and illite/montmorillonite/quartz mixtures. However, the strength degradation was observed to be almost linear in the illite/quartz mixture, not showing any drastic drops that may be identified with the transitions between three regimes. The difference in behavior may be related to the fact the illite/quartz mixture has the highest hardening rate and yet the strength contrast between the two end-members (of quartz and illite) is the lowest.

5.3. Ternary Diagram for Frictional Strength of Simulated Gouge Mixtures and Application to Natural Gouges

[55] This study has demonstrated that the friction coefficient is dependent on clay content as well as clay mineralogy. To constrain the frictional strength of a seismogenic setting made up of clay-rich fault gouge, we will use a ternary plot for

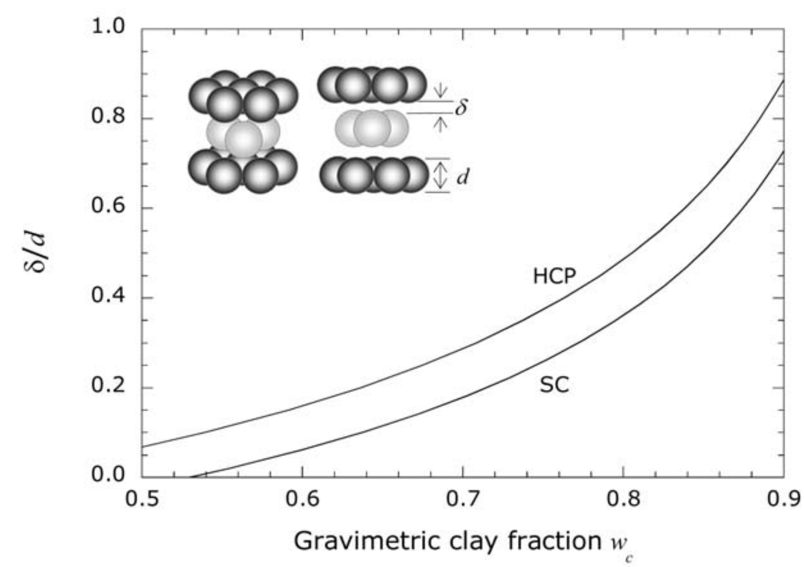

Figure 13. The normalized clay thickness versus the clay content for simple cubic (SC) packing and hexagonal close packing where δ is the layer spacing and d is the diameter of a spherical quartz particle.

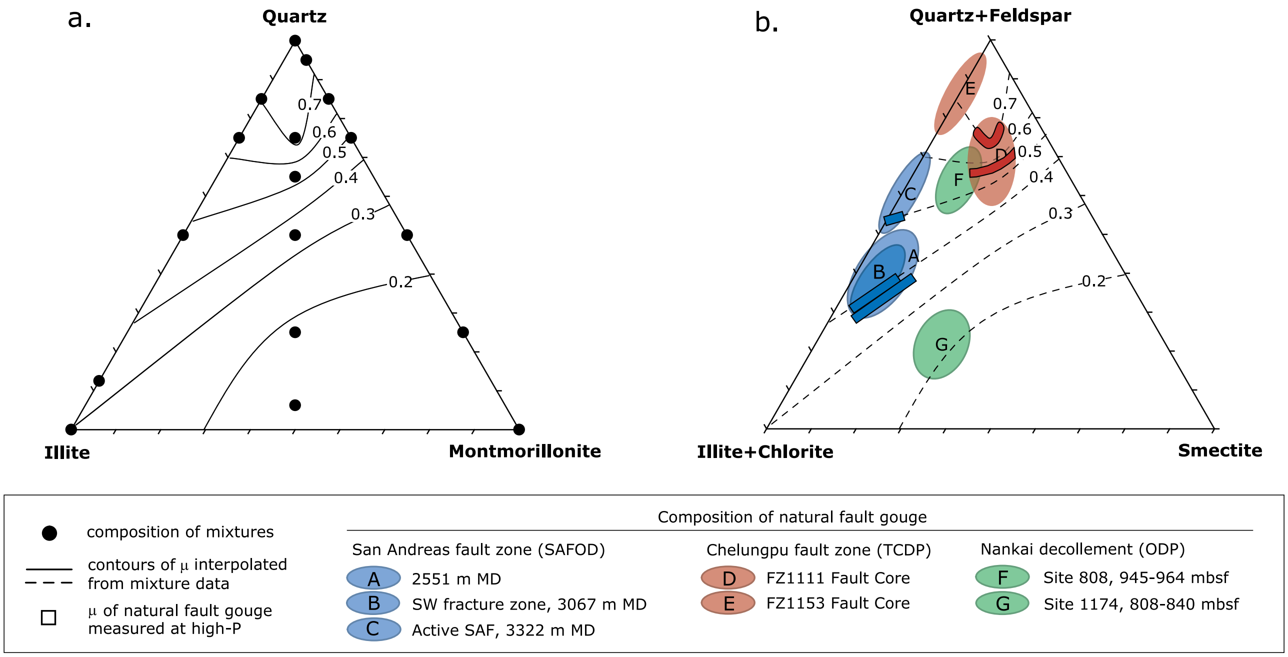

Figure 14. (a) Compositions of simulated clay-quartz gouges are plotted as black circles. Each point is associated with a friction coefficient which then was used to construct contours. (b) For comparison, we plot the compositions of natural shear zone samples retrieved by drilling projects (colored areas). The measured range of friction coefficients for the natural samples is represented by the bars. SAFOD data are from *Solum et al.* [2006] and *Morrow et al.* [2007]. TCDP data are from *Kuo et al.* [2005] and unpublished data. ODP data for Sites 808 and 1174 are from *Underwood et al.* [1993] and *Steurer and Underwood* [2003], respectively.

empirical interpolation of our laboratory data for various synthetic gouge mixtures. Our data on binary and ternary mixture are compiled in such a ternary diagram in Figure 14a. The black circles mark the compositions of the synthetic mixtures used in our experiments. Each point is associated with a friction coefficient (compiled in Table 1) at axial displacement of 7.98 mm. Interpolation of these data points maps out the compositional variation of friction coefficient, and accordingly each point inside the ternary diagram is assigned a unique value for its friction coefficient. Contours can then be drawn connecting points with constant friction coefficients. Such iso-friction contours for coefficient values of 0.2–0.7 (at increments of 0.1) are plotted in Figure 14a. If the dependence of frictional strength on clay content were linear, the contours would be straight lines. However, with the exception of the illite/quartz mixture, the dependence was observed to be nonlinear involving three regimes in the mixtures studied, and consequently the contours derived are curvilinear.

[56] To compare with core samples retrieved from fault zones, we reproduce the iso-friction contours (constrained by data of synthetic gouge mixtures) as the dashed curves in Figure 14b. In recent years, several drilling projects have investigated active fault zones in a variety of tectonic settings and retrieved core for laboratory study. We compile data for clay-rich fault gouge obtained by deep drilling programs for three major shear zones: The San Andreas fault, Chelungpu fault, and Nankai décollement. As detailed below, the mineral compositions of the samples are indicated by the shaded ellipses. The size of the ellipse is due to the spread in composition of the samples and uncertainty in the determination method. Where possible we have also included the friction coefficient determined by high-pressure experiments of gouge samples retrieved from these drilling sites. With reference to the synthetic mixture data (Figure 14a), the upper and lower limits of friction coefficients of these fault zone materials define two curvilinear contours. The region bounded by the intersection of these two contours with the shaded composition ellipse is marked by the thick colored bars in Figure 14b. If the friction coefficients of the fault samples and synthetic samples were fundamentally different, then the upper and lower iso-friction contours would not intersect the composition ellipse anywhere in the ternary diagram.

[57] The SAFOD penetrated the creeping section of the fault in 2006 and is currently probing a region of repeating seismicity. The SAFOD main hole passed through numerous shear zones, including at least one actively deforming trace of the San Andreas fault. *Solum et al.* [2006] distinguished five shear zones from bulk mineral assemblages sampled in drill core and cuttings collected during the project's first two phases. Of these only three, from 2545 to 2560 m MD, the extended fracture zone at 3067 m MD, and the inferred actively deforming zone at 3310–3353 m MD [*Hickman et al.*, 2005], were abundant in illite, chlorite, and mixed layer illite-smectite clay phases. The remaining two shear zones were enriched in laumontite and contained only trace amounts of clay so they were not included in our diagram. Although it is unclear how chlorite would behave in a mixture, given that the friction coefficient of chlorite is about 0.4 under saturated conditions [*Morrow et al.*, 2000], we felt it more appropriate

to lump it with the illite fraction rather than the montmorillonite. Undoubtedly, there will be some error in estimating the friction coefficient, which can only be mitigated by a study on chlorite mixtures. For comparison, we show data from saw cut frictional sliding tests conducted by *Morrow et al.* [2007] and *Tembe et al.* [2006] on SAFOD gouge materials at 40 MPa effective normal stress. The shaded areas indicate mineralogy determined by XRD analyses [*Solum et al.*, 2006; *Morrow et al.*, 2007], while the bars represent friction data. Samples A and C from 2551 and 3322 m MD, respectively, contained up to 27 wt.% chlorite and were obtained using a method developed by *Morrow et al.* [2007] in which only drill cuttings containing slickensides were tested. This ensured the weak shear zone material would not be diluted by the surrounding bulk material and in doing so yielded data better representative of the shear zone. *Tembe et al.* [2006] investigated the frictional behavior of the 3067 m MD SAFOD drill core (plotted as sample B) which contained 62%–69% illite and mixed illite/smectite phases. Velocity strengthening behavior was reported for all the SAFOD samples.

[58] The TCDP drilled two boreholes into the Chelungpu fault that ruptured 1999 Mw7.6 Chi-Chi earthquake. Two potential shear zones for slip in the 1999 event were identified at 1111 and 1153 m in TCDP Hole A. The core samples for these depths are included in Figure 14 as samples D and E, respectively. *Kuo et al.* [2005] conducted XRD clay mineral analyses of the shear zone materials. They reported a thin-black layer rich in smectite and illite in the fault core at 1111 m. All other clay phases are absent or present at low concentrations. Illite and chlorite were present in the deeper shear zone, while smectite and kaolinite phases were entirely absent. In Figure 14, shaded ellipses indicate the composition of the fault cores. Triaxial saw cut tests conducted on water-saturated gouge at 18 MPa effective confining pressure from FZ1111 obtained friction coefficients of 0.55–0.6.

[59] The Nankai décollement has been extensively studied by the ODP and Deep Sea Drilling Program (DSDP) and much like the San Andreas, shares the common attribute of appearing extremely weak despite being locked through much of its length. The Nankai accretionary prism was formed with subduction of the Philippine Plate (Shikoku Basin) following periods of seafloor spreading and volcanism [*Shipboard Scientific Party*, 2001a and references therein]. The basal décollement of the Nankai accretionary wedge occurs in the lower Shikoku Basin facies consisting of hemipelagic mudstones and claystones, volcanic ash and replacement of vitrified glass with smectite and zeolites [*Shipboard Scientific Party*, 2001b]. The décollement was penetrated near the toe of the subduction zone at ODP Sites 808 and 1174 at depths of 945–964 m below seafloor and at 808–840 m below seafloor, respectively. *Underwood et al.* [1993] found illite to be the dominant clay phase with total clay fraction of about 30 wt.% at Site 808, whereas Site 1174 about 250 km away was reported to have up to 90% clay [*Steurer and Underwood*, 2003]. Ring-shear experiments at pressures <2 MPa by *Kopf and Brown* [2003] obtained values of about 0.2 for the ODP décollement zone in general agreement with our estimates at 40 MPa for a clay-rich shear zone.

[60] Constrained by systematic measurements on synthetic gouge mixtures, we derived iso-friction contours in a ternary diagram. Laboratory data on upper and lower limits of friction coefficients of core samples from fault drilling projects can then be identified with two such contours. We found that for the SAFOD, TCDP, and Nankai ODP core samples, these upper and lower contours intersect the composition ellipses in specific regions inside the ternary diagram, thus demonstrating that empirically interpolated contours based on synthetic mixture measurements (Figure 14a) can be used to estimate the frictional strength of a fault zones simply on the basis of its clay composition.

[61] We note the majority of samples are from mature fault zones and belong to a regime (with 20–70% clay) in which strength degradation is greatest and the development of foliation as a failure mode is active. In this transitional regime, the frictional strength deviates considerably from the prediction of Byerlee's rule for a gouge dominated by siliciclastic minerals with relatively low clay content. This is also the regime in which the frictional strength is highly sensitive to variations in clay content. In this study, we have restricted ourselves to room temperature conditions; however, a deeper understanding of these related phenomena requires systematic experiments at a range of elevated pressure and temperature conditions relevant to seismogenic depths.

6. Summary and Conclusions

[62] We systematically investigated the frictional sliding behavior of simulated quartz-clay gouges at seismogenic stress conditions. Conventional triaxial compression tests were conducted on saturated saw cut samples containing binary and ternary mixtures made up of quartz, montmorillonite, and illite clays. In all three systems, there was an overall decrease in strength with increasing clay content and the friction coefficient ranged between the end-member values of 0.75 for quartz, 0.303 and 0.17 for the illite and montmorillonite clay, respectively. If taken at a single displacement, the illite/quartz system generally followed a linear trend of strength reduction with increasing clay content, while in montmorillonite-bearing mixtures the reduction in strength was nonlinear and could be characterized by three regimes of high strength, low strength, and transitional.

[63] Microstructural observations were performed on the deformed samples to characterize the geometric attributes of shear localization within the gouge layers. Distinct textures involving the development of Riedel shears and clay foliation were identified in samples deformed to comparable strains. The textures which were observed in all three systems appeared to depend on clay content and coincided with changes in strength. Two micromechanical models were adopted to analyze the transitions from regimes 1 to 2 and from 2 to 3. The first transition follows from the ideal packing model and is associated with the shift from a stress-supporting framework of quartz grains to a clay matrix-supporting framework. In the microstructure, the transition is manifested by the development of P-foliation and reduction in Riedel shear angle. The second transition (from regime 2 to 3) is attributed to the development of shear localization in the clay matrix which can develop only when the nearby layers of quartz grains are sufficiently separated. Analytic estimates of the critical clay thickness between neighboring quartz grains were obtained from a conceptual model in

which the gouge is treated as an assemblage of randomly or regularly packed quartz grains embedded in a clay matrix.

[64] The three-regime model developed by *Lupini et al.* [1981] was based on low normal stress data in which residual strength had been reached and grain crushing and comminution were negligible. At high normal stress, grain crushing becomes an important mechanism for strain hardening and given the triaxial geometry with its inherent limitation on total slip, strength data during strain hardening should be compared only at similar slip distances or shear strains. Comparison with published high-stress data at similar displacements demonstrated the friction coefficient may be a linear to nonlinear function of clay content.

[65] Friction data collected on synthetic gouge mixtures were compared to data on natural clay shear zone materials obtained by scientific deep drilling projects. The natural gouges from shear zones were moderately weak to strong and mostly belonged to the transitional regime between high and low strength. Experiments conducted at high pressures on the natural samples obtained friction coefficients that were in accord with estimates from synthetic mixtures.

Appendix A: Corrections to Recorded Stresses and Coefficient of Friction

[66] In nearly all laboratory measurements of rock or gouge friction, regardless of test geometry, total force or torque is one of the measured quantities. Adjustments to these total force measurements are then computed for seal friction and jacket strength to determine the actual stresses applied to the sample. The continuing demand for improved accuracy, especially when replicating low-stress conditions appropriate for the shallow crust, has required continued improvement in understanding sources of error in determining applied stress. In this appendix, we discuss the most significant sources of error when measuring coefficient of friction in the triaxial test geometry used in this study. While other recent studies [i.e., *Ikari et al.*, 2009] have raised concerns of the accuracy of triaxial friction tests, we would point out that similar problems exist for all test configurations. For example, the *Ikari et al.* [2009] study was conducted on a “double direct shear” apparatus modified to include a pressure chamber to apply confinement to the test sample. This geometry requires correction for seal friction between the loading pistons and the pressure chamber, correction for the rubber jacketing separating the sample from the confining fluid, and thinning of the gouge sample that occurs at large strains. These are the very same corrections that need to be determined for the triaxial test geometry. While among other issues, *Ikari et al.* assert that “sample cocking” may be a source of error in determine stress state in the triaxial geometry, to our knowledge, no observations exist that demonstrate the magnitude or even the existence of this effect.

[67] Many of the corrections that are considered in this section have already been reported on, for example, by *Moore and Lockner* [2007] for high temperature friction measurements. At elevated temperature, jacket strength corrections are a more serious problem since metal jackets that have significant shear strength must be used. (In the most severe cases at elevated temperature, shear stress corrections of as much as 9 MPa must be applied.) We will restrict our observations to room temperature measurements as used in this study where stress corrections for jacket strength are typically between 0 and 1 MPa. Fundamental measurements used in computing stress are axial force F_{axial} (converted to axial stress σ_1), axial displacement dl and confining pressure P_c. Uncorrected axial stress is simply $\sigma_1 = F_{\text{axial}}/\pi r^2$, where r is sample radius. For the triaxial geometry, intermediate and minimum principal stresses are $\sigma_2 = \sigma_3 = P_c$. Then, uncorrected shear and normal stress components resolved on the saw cut plane (Figure 2) are given by the familiar formulas

$$\tau = \frac{1}{2}(\sigma_1 - P_c)\sin 2\psi \tag{A1}$$

$$\sigma_n = \frac{1}{2}[(\sigma_1 + P_c) - (\sigma_1 - P_c)\cos 2\psi], \tag{A2}$$

where ψ is the angle between the sample axis and the fault plane (in our case, $\psi = 30°$).

A1. Seal Friction

[68] Axial force applied to the sample is commonly measured with a load cell located outside of the pressure vessel. In this case, some portion of the measured force is resisted by friction between the moving piston and the confining pressure seal assembly. In the experiments reported here, a second load cell that was located inside the pressure vessel was used to measure axial force. By using this internal load cell, there is no correction required for seal friction.

A2. True Area of Contact

[69] Sliding surfaces of the granite and sandstone driving blocks (Figure 2) are formed by cutting 25.4 mm diameter rock cylinders at an angle of 30° to the sample axis. The resulting sliding surfaces are ellipses with a 2:1 aspect ratio. A 1 mm thick gouge layer is placed between sliding surfaces with the axes of the upper and lower driving blocks initially aligned. As the piston is advanced, slip is induced within the gouge layer causing the lower driving block to shift laterally as well as vertically. Thus, as sliding continues, the true contact area that supports shear and normal tractions steadily decreases. The reduction in contact area can be related to the axial shortening [*Scott et al.*, 1994] by considering the formula for the area of overlap between two offset circles of equal radius:

$$A/A_0 = (\Theta - \sin\Theta)/\pi \tag{A3}$$

$$\Theta = \pi - 2\sin^{-1}[(dl/2r)\tan\psi], \tag{A4}$$

where A_0 and A are the original and corrected cross-sectional areas of the sample and other variables are defined in section 3.2 and Appendix A. Θ is the angle subtended by the points of intersection of two overlapping circles, at the centers of the circles. Then, the “true” shear and normal stress components are computed by dividing the uncorrected stresses by the factor A/A_0. In this study, axial shortening was stopped at 8 mm (9.2 mm resolved on the fault surface). By 8 mm, the area correction results in a stress adjustment of 23%. This

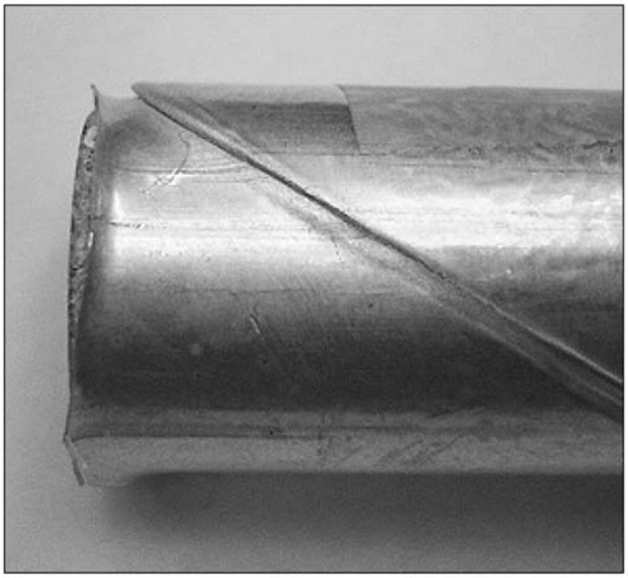

Figure A1. Unlike samples run with polyurethane jackets that back slip when confining pressure is removed, this silver-jacketed sample has preserved the deformation structure at the end of the experiment. Note that the jacket wraps around the tip of the sample and immobilizes gouge that has left the contact region between the driving blocks. Also, note that no gouge has extruded laterally from the shear zone. These features are consistent with the true-area-of-contact stress correction used in this study. The gouge thickness is 1 mm.

contact area correction was updated continually during the experiments and applied on-the-fly to computed normal stress. All tests were run under computer control to maintain constant effective normal stress based on this calculation.

[70] Another possible area correction is related to the fact that many of the clay-rich gouge samples have low strength so that as shearing progresses, gouge might extrude from between the driving blocks and result in the load-bearing contact area being different from the assumed overlapping ellipses of the forcing blocks. It is difficult to preserve the final gouge configuration in samples with rubber jackets due to jacket rebound. However, shown in Figure A1 is a gouge saw cut sample deformed with a thin-walled silver jacket that has preserved characteristics of a typical deformation test. A portion of the gouge adhered to the sliding surface as it moved out of the contact region between the driving blocks and was trapped between the exposed portion of the driving block and the jacket. This means that the localized slip surface has remained between the two driving blocks and has not extended into the portion of gouge outside of the contact area. Also, normal stress is applied by the driving blocks and once gouge moves out of the high-stress region, stress is reduced and the gouge becomes weaker. This configuration, which is confirmed by thin section observations, is consistent with the area correction presented in this section. Furthermore, no gouge is extruded out of the shear zone in a direction perpendicular to shearing. This observation is also consistent with the area correction presented here.

A3. Jacket Strength

[71] We have performed numerous calibration runs to determine the shear resistance of the jacketing materials used in our experiments. High temperature jacket strength corrections are discussed most recently by *Moore and Lockner* [2007]. For limited displacements and temperature up to 250°C, lead is our preferred jacketing material. Lead has low strength and minimal strain hardening so that strength corrections are small. For room temperature tests at confining pressure up to 200 MPa, we now prefer to use latex jackets because of their low strength. However, the sand-clay mixture experiments shown here were carried out when we were still using a combination of a polyolefin sleeve to stabilize the sample during assembly and an outer polyurethane sleeve to exclude the confining fluid. Other researchers have used multiple layers of polyolefin sleeves to jacket their samples. For our high-pressure experiments, we prefer to use polyurethane sleeves. Our tests indicate that a 5 mm thick polyurethane sleeve has less shear resistance than a single layer of 0.9 mm thick polyolefin tubing. Furthermore, polyurethane is impermeable to most petroleum-based fluids and remains elastic to pressures greater than 500 MPa.

[72] Determining the shear strength correction appropriate for a given jacketing material has been an ongoing process. The basic approach has been to deform a sample that has low and nearly constant shear resistance so that the displacement-dependent contribution of jacket strength could be measured directly. We have used, for example, greased Teflon shims between polished steel driving blocks, greased and ungreased indium and lead shims between steel driving blocks, and wet talc gouge layers between sandstone driving blocks. Wet talc is a preferred standard at elevated temperature since it has nearly constant friction over a broad temperature range [*Moore and Lockner*, 2007]. When the experiments reported in this study were performed, jacket strength was calibrated by shearing greased Teflon wafers between polished steel forcing blocks. Apparent shear stress resolved parallel to the 30° slip surface increased steadily with slip. A least squares fit gave a slope of $\Delta\tau/\Delta l$ = 0.065 MPa/mm. This correction, proportional to axial shortening, was applied to all raw shear stress measurements in this study. At 8 mm displacement, shear stress was lowered by 0.52 MPa and the corresponding coefficient of friction in all tests was reduced by 0.013.

A4. Lateral Slip of Lower Driving Block

[73] In the triaxial configuration, fault-parallel shear must be accompanied by lateral motion of the lower driving block. This lateral motion is accommodated by slip between the steel end cap and the piston (Figure 2). A force balance analysis indicates that shear traction on the piston face imposes additional forces on the saw cut. Normal stress on the saw cut face is increased by $\frac{1}{2}\tau_b$ $(1 - \cos 2\psi)$, where τ_b is the shear stress developed at the piston-end cap interface. Shear stress on the saw cut is reduced by $\frac{1}{2}\tau_b$ $(1 - \cos 2\psi)$. To minimize this effect, a greased Teflon shim is placed between the piston and steel end cap (Figure 2). This shim has the same frictional properties as the greased Teflon used in the jacket strength calibration tests. Therefore, the shear resistance of the Teflon shim can be determined from

the zero-displacement intercept in a jacket strength calibration test. In this way, we estimate that the yield stress for lateral motion on the piston face imposes an approximately constant 0.4 MPa normal stress on the saw cut surface and reduces shear stress by approximately 0.25 MPa. The 0.4 MPa normal stress correction was applied to all friction data, although the 0.25 MPa shear stress adjustment was not. Application of the shear stress adjustment would reduce all friction values by 0.006, a correction that is relatively small and within the absolute error of the friction determinations. For the purposes of this study, relative differences in friction are most important. In this case, a constant offset of all friction values does not affect relative changes in friction.

[74] For the different stress corrections applied in this study, only the fault contact area reduction scales with applied normal stress. At 8 mm displacement, this results in an increase of 23% in both shear and normal stress. Consequently, the coefficient of friction, which is the ratio of shear to normal stress, is relatively insensitive to errors in this correction term. Our calibration tests indicate that jacket strength and lateral slip corrections are, to first order, insensitive to normal stress or confining pressure. At 8 mm displacement, these are considered constant offsets in stress, regardless of the applied normal stress. Thus, they become less significant in affecting the measurement of the friction coefficient as normal stress is increased. At 8 mm axial shortening, jacket strength and lateral slip corrections reduce μ by approximately 0.01 each. Similar tests run at 100 MPa normal stress would, for comparison, result in corrections to μ of about 0.005.

A5. Stiffness Corrections

[75] We end this section with a comment on the difference between measured axial shortening, fault slip, and loading/unloading slope. The horizontal axis in Figure 3 is axial shortening adjusted for elastic distortion of the loading frame and driving blocks. In these experiments, a transducer measures the change in distance between the ram and the pressure vessel. This measurement includes displacement in the gouge layer as well as changes in length of the driving blocks, the steel piston, tie rods, and other members of the loading frame. Advancing the ram without slip on the saw cut surface results in an increase in σ_1, σ_n, and τ. The control system responds by reducing confining pressure to return normal stress to the preset value. The rise in stress is determined by the stiffness of the loading frame and sample assembly. The sample gouge layer, which typically compacts to about 0.5 mm, provides only a minor contribution to the overall system stiffness. By running constant normal stress calibration tests on both steel and rock samples (without gouge), we have determined that the loading frame and granite/sandstone forcing blocks contribute approximately equal portions to the system stiffness. In terms of friction coefficient, we express stiffness as $k\mu = \Delta\mu/\Delta l$. Then, we measured total system stiffness of $k_{\mu,\mathrm{total}} = 3.1\ \mathrm{mm}^{-1}$ and stiffness of the loading frame without driving blocks of $k_{\mu,\mathrm{machine}} = 6.2\ \mathrm{mm}^{-1}$. To remove the elastic response of the loading frame and driving blocks, measured displacement is reduced by $\mu/k_{\mu,\mathrm{total}}$. This adjusted axial shortening is plotted as the horizontal axis in Figure 3. Initial slopes in the first 0.25 mm of displacement in Figure 3 are typically 1.4 mm^{-1} and represent a combination of gouge compaction and shearing. In any event, small errors in slip of the gouge layer have little effect on our calculations of relative gouge strength since the observed strain hardening slopes are small.

Appendix B: An Ideal Packing Model for Frictional Strength Degradation

[76] With reference to Figure 12, the transition from regime 1 to 2 as envisioned by *Lupini et al.* [1981] is associated with a qualitative change in the grain packing, from a mixture with an interconnected framework of quartz grains supporting the applied stresses to one with an interconnected clay matrix. Such a transition can be analyzed using results from powder technology on the packing of a binary mixture of fine and coarse particles [*McGeary*, 1961; *Cumberland and Crawford*, 1987], which have provided useful insights into the mechanical compaction, seismic velocity, and permeability of a sand-clay mixture as functions of porosity and pressure [*Marion et al.*, 1992; *Koltermann and Gorelick*, 1995; *Revil et al.*, 2002; *Crawford et al.*, 2008].

[77] According to this ideal packing model, the mixture in regime 1 can be considered to form in two steps. The quartz grains are first assembled to form an interconnected, stress-supported framework that has an interstitial void space with porosity ϕ_s. The clay particles are then randomly added into the void space without disturbing the pre-existing quartz framework. As the clay content increases, a point will be reached when all the interstitial space has been filled, and further addition of clay particles necessitate the breakage of existing quartz grain contacts, which would enhance the connectivity among the clay grains and development of an interconnected clay matrix at the inception of regime 2. If we define the volumetric clay fraction c as the ratio of the volume of dry clay (which includes the volumes of solid clay grains and pore space) to that of the dry gouge mixture, then one would conclude that the transition from regime 1 to 2 occurs when clay grains fill up all the interstitial volume corresponding to the porosity ϕ_s, i.e., when

$$c = \phi_s. \tag{B1}$$

[78] In most laboratory studies, the clay content is characterized by the weight or gravimetric fraction w_c, which is related to the volumetric clay fraction c by

$$w_c = \frac{c(1-\phi_{cl})}{c(1-\phi_{cl}) + (1-\phi_s)(\rho_s/\rho_{cl})} \quad \text{for } c \le \phi_s \tag{B2}$$

$$w_c = \frac{c(1-\phi_{cl})}{c(1-\phi_{cl}) + (1-c)(\rho_s/\rho_{cl})} \quad \text{for } c \ge \phi_s, \tag{B3}$$

where ϕ_{cl} denotes the porosity of the dry clay grains, and ρ_s and ρ_{cl} denote the grain densities of quartz and clay, respectively [*Marion et al.*, 1992]. We will follow *Revil et al.* [2002] to take $\rho_s \approx \rho_{cl} \approx 2650\ \mathrm{kg\ m^{-3}}$ and accordingly assume $\rho_s/\rho_{cl} = 1$. This assumption is applicable here since we determined the weight fraction on clay minerals that had been dried in vacuo under elevated temperature to remove their bound water. If the clay minerals had water adsorbed on the surface, the density ρ_{cl}, could be appreciably lower. The gravimetric clay fraction at the transition from regime 1 to 2 corresponding to the critical condition (B1) is given by

$$w_{cr} = \frac{(1-\phi_{cl})}{(1-\phi_{cl}\phi_s)}\phi_s. \quad \text{(B4)}$$

Appendix C: Frictional Strength Degradation Associated With a Critical Thickness of Clay Layer

[79] It was postulated by *Lupini et al.* [1981] that the inception of their regime 3 hinges on the attainment of a critical thickness for the clay layer that separates two neighboring layers of sand grains. Here we explicitly derive some of the results for this scenario. First-order estimates of the geometric attributes involved can be derived for the idealized model of monodisperse spheres randomly (Figure 12a) or regularly packed (Figure 12b). We will first consider the random case using *Chandrasekhar*'s [1943] elegant result that the mean of the nearest neighbor distance between a random distribution of particles is

$$\lambda = \Gamma(4/3)/(4\pi n/3)^{1/3} = 0.554 n^{-1/3}, \quad \text{(C1)}$$

where Γ is the factorial function and n denotes the number of particles per unit volume. If we assume that the particles are quartz with a mean diameter d, then the volumetric fraction of quartz is $\pi n d^3/6$ and the volumetric clay fraction is $c = 1 - \pi n d^3/6$ which implies that

$$n = \frac{6}{\pi}\frac{(1-c)}{d^3}. \quad \text{(C2)}$$

Substituting (C1) into (C2), we obtain

$$\lambda = 0.554 d\left(\frac{\pi}{6(1-c)}\right)^{1/3}. \quad \text{(C3)}$$

The minimum requirement for the existence of a continuous clay layer between nearest neighbors of quartz particles is $\lambda > d$, which from (C3) requires $c > 1 - (\pi/6)\ 0.554^3 = 0.911$. While this is a rather general result, it provides an estimate that is overly conservative in that our observations indicate that the transition from regime 2 to 3 occurs at a critical clay fraction appreciably lower than 91%.

[80] This suggests that we should consider a more close-packed configuration. As a first example, we will consider monodisperse spheres (with diameter d and radius $r = d/2$) in a HCP assemblage (Figure 12b). With the spherical quartz grains in contact (corresponding to the scenario at the transition from regime 1 to 2 analyzed in Appendix B), the unit cell volume for HCP is $V = 4\sqrt{2}r^3$, and since the volume of the sphere is $4/3\ \pi r^3$ the clay volume is $V - 4/3\ \pi r^3$ and the volumetric clay fraction is $c = \phi_s = 1 - \pi/(3\sqrt{2}) = 0.26$ [*Cumberland and Crawford*, 1987; *Mavko et al.*, 1998]. We note that this value is close to the estimate of $\phi_s \approx 25\%$ for our montmorillonite/quartz mixtures at the transition from regime 1 to 2. To analyze the progressive increase of clay content in regime 2, we will assume that the clay increments are distributed homogenously and model it as the superposition of two steps. In the first step, we consider a uniform dilation of the system so that the linear dimension is increased by a factor of $\alpha > 1$. This dilation results in solid grains with radius $R = \alpha r$ embedded in unit cells of volume $V = 4\sqrt{2}R^3$. In the second step, the solid grains are allowed to shrink back to the initial radius of r, and the void space created is filled with clay. At the end of these two steps, the volume of the sphere remains $4/3\ \pi\ r^3$, but the volumetric clay fraction has increased to

$$c = 1 - \frac{\pi}{(3\sqrt{2})}\left(\frac{r}{R}\right)^3 = 1 - 0.740/\alpha^3. \quad \text{(C4)}$$

[81] For a given α equations (C4) and (B3) can be used to calculate the gravimetric clay fraction w_c. A clay layer of uniform thickness will now separate two adjacent layers of spherical grains in such a regular packing. At the end of the first step (with the dilated grains in contact with one another), the layer spacing in the HCP system of spherical grains is $2\sqrt{2/3}\ R$ [*Cumberland and Crawford*, 1987]. After the grains have contracted back to radius r in the second step, a clay layer of uniform thickness $\delta = 2\sqrt{2/3}\ R - 2r = 2(\sqrt{2/3}\ \alpha - 1)r$ is incorporated to fill in the gap. *Lupini et al.* [1981] proposed using the ratio $\delta/d = \delta/(2r)$ as the geometric parameter that controls the transition from regime 2 to 3. Specifically for the HCP system we analyze here, this ratio is given by

$$\delta/d = \sqrt{2/3}\alpha - 1 = 0.816\alpha - 1. \quad \text{(C5)}$$

As a second example, we consider the SC packing which is relatively loose. For this configuration with volume $V = 8r^3$ and layer spacing $2r$, the volumetric clay fraction and normalized clay layer thickness are given by

$$c = 1 - \pi/\left(6\alpha^3\right) = 1 - 0.524/\alpha^3 \quad \text{(C6)}$$

$$\delta/d = \alpha - 1. \quad \text{(C7)}$$

Figure 13 plotting the normalized clay layer thickness δ/d as a function of w_c for these two packing arrangements was calculated assuming $\phi_{cl} = 0.24$ in equation (B3) and using the expressions for c in (C4) and (C6) for the HCP and SC configurations, respectively.

[82] **Acknowledgments.** We have benefited from discussions with Diane Moore, Carolyn Morrow, and Nick Beeler and reviews by Chris Spiers and Chris Marone. We also thank John Solum for conducting the XRD analyses. Li-Wei Kuo and Sheng-Rong Song shared with us their TCDP data. Brian Crawford kindly provided us with his unpublished manuscript on kaolinite-quartz mixtures. ST was supported by a DoEd GAANN fellowship. This research was partially supported by U.S. National Science Foundation under grant EAR-0346022.

References

Biegel, R. L., C. G. Sammis, and J. H. Dieterich (1989), The frictional properties of a simulated gouge having a fractal particle distribution, *J. Struct. Geol.*, *11*, 827–846.

Brown, K. M., A. Kopf, M. B. Underwood, and J. L. Weinberger (2003), Compositional and fluid pressure controls on the state of stress on the Nankai subduction thrust: A weak plate boundary, *Earth Planet. Sci. Lett.*, *214*, 589–603, doi:10.1016/S0012-821X(03)00388-1.

Byerlee, J. D. (1978), Friction of rocks, *Pure Appl. Geophys.*, *116*, 615–626.
Chandrasekhar, S. (1943), Stochastic problems in physics and astronomy, *Rev. Mod. Phys.*, *15*(1), 1–89.
Crawford, B. R., D. R. Faulkner, and E. H. Rutter (2008), Strength, porosity, and permeability development during hydrostatic and shear loading of synthetic quartz-clay fault gouge, *J. Geophys. Res.*, *113*, B03207, doi:10.1029/2006JB004634.
Cumberland, D. J., and R. J. Crawford (1987), *The Packing of Particles*, 148 pp., Elsevier, Amsterdam.
Dieterich, J. H. (1979), Modeling of rock friction: 1. Experimental results and constitutive equations, *J. Geophys. Res.*, *84*, 2161–2168.
Gu, Y., and T.-F. Wong (1994), Development of shear localization in simulated quartz gouge: Effect of cumulative slip and gouge particle size, *Pure Appl. Geophys.*, *143*, 387–424.
Hickman, S. H., M. D. Zoback, and W. L. Ellsworth (2005), Structure and composition of the San Andreas Fault Zone at Parkfield: Initial results from SAFOD phases 1 and 2, *EOS Trans. AGU*, *86*(52), Fall Meet. Suppl., Abstract T23E-05.
Ikari, M. J., D. M. Saffer, and C. Marone (2007), Effect of hydration state on the frictional properties of montmorillonite-based fault gouge, *J. Geophys. Res.*, *112*, B06423, doi:10.1029/2006JB004748.
Ikari, M. J., D. M. Saffer, and C. Marone (2009), Frictional and hydrologic properties of clay-rich fault gouge, *J. Geophys. Res.*, *114*, B05409, doi:10.1029/2008JB006089.
Koltermann, C. E., and S. M. Gorelick (1995), Fractional packing model for hydraulic conductivity derived from sediment mixtures, *Water Resour. Res.*, *31*(12), 3283–3297.
Kopf, A., and K. M. Brown (2003), Friction experiments on saturated sediments and their implications for the stress state of the Nankai and Barbados subduction thrust, *Mar. Geol.*, *202*(3–4), 193–210.
Kuo, L., S. Song, and H. Chen (2005), Characteristics of clay minerals in the fault zone of TCDP and its implications, *Eos Trans. AGU*, *86*(52), Fall Meet. Suppl., Abstract T43D-05.
Lockner, D. A., and N. M. Beeler (2002), Rock failure and earthquakes, in *International Handbook of Earthquake and Engineering Seismology*, edited by W. H. K. Lee et al., pp. 505–537, Academic, Amsterdam.
Logan, J. M., and K. A. Rauenzahn (1987), Frictional dependence of gouge mixtures of quartz and montmorillonite on velocity, composition and fabric, *Tectonophysics*, *144*, 87–108.
Logan, J. M., M. Friedman, N. Higgs, C. Dengo, and T. Shimamoto (1979), Experimental studies of simulated gouge and their application to studies of natural fault zones, *U.S. Geol. Surv. Open-File Rep.*, *79-1239*, 305–343.
Logan, J. M., C. A. Dengo, N. G. Higgs, and Z. Z. Wang (1992), Fabrics of experimental fault zones: Their development and relationship to mechanical behavior, in *Fault Mechanics and Transport Properties of Rocks*, edited by B. Evans and T.-F. Wong, pp. 33–67, Academic, San Diego, Calif.
Lupini, J. F., A. E. Skinner, and P. R. Vaughan (1981), The drained residual strength of cohesive soils, *Geotechnique*, *31*, 181–213.
Marion, D., A. Nur, H. Yin, and D. Han (1992), Compressional velocity and porosity in sand-clay mixtures, *Geophysics*, *57*, 554–363.
Mavko, G., T. Mukerji, and J. Dvorkin (1998), *The Rock Physics Handbook: Tools for Seismic Analysis in Porous Media*, pp. 147–161, Cambridge Univ. Press, Cambridge, U.K.
McGeary, R. K. (1961), Mechanical packing of spherical particles, *J. Am. Ceram. Soc.*, *44*(10), 513–522.
Moore, D. E., and D. A. Lockner (2004), Crystallographic controls on the frictional behavior of dry and water-saturated sheet-structure minerals, *J. Geophys. Res.*, *109*, D15S15, doi:10.1029/2003JD003543.
Moore, D. E., and D. A. Lockner (2007), Friction of the smectite clay montmorillonite: A review and interpretation of data, in *The Seismogenic Zone of Subduction Thrust Faults*, *MARGINS Theor. Exp. Earth Sci. Ser.*, vol. 2, edited by T. H. Dixon and J. C. Moore, pp. 317–345, Columbia Univ. Press, New York.
Moore, D. E., R. Summers, and J. D. Byerlee (1989), Sliding behavior and deformation textures of heated illite gouge, *J. Struct. Geol.*, *11*, 329–342.
Morrow, C., J. Solum, S. Tembe, D. Lockner, and T.-f. Wong (2007), Using drill cutting separates to estimate the strength of narrow shear zones at SAFOD, *Geophys. Res. Lett.*, *34*, L11301, doi:10.1029/2007GL029665.
Morrow, C. A., B. Radney, and J. D. Byerlee (1992), Frictional strength and the effective pressure law of montmorillonite and illite clays, in *Fault Mechanics and Transport Properties of Rocks*, edited by B. Evans and T.-F. Wong, pp. 69–88, Academic, San Diego, Calif.
Morrow, C. A., D. E. Moore, and D. A. Lockner (2000), The effect of mineral bond strength and adsorbed water on fault gouge frictional strength, *Geophys. Res. Lett.*, *27*, 815–818.
Paterson, M. S., and T.-F. Wong (2005), Friction and sliding phenomena, in Experimental Rock Deformation: The Brittle Field, edited by M. S. Paterson and T.-F. Wong, pp. 165–210, Springer, New York.
Revil, A., D. Grauls, and O. Brévart (2002), Mechanical compaction of sand/clay mixtures, *J. Geophys. Res.*, *107*(B11), 2293, doi:10.1029/2001JB000318.
Saffer, D. M., and C. Marone (2003), Comparison of smectite- and illite-rich gouge frictional properties: Application to the updip limit of the seismogenic zone along subduction megathrusts, *Earth Planet. Sci. Lett.*, *215*(1–2), 729–736.
Scott, D. R., D. A. Lockner, J. D. Byerlee, and C. G. Sammis (1994), Triaxial testing of Lopez fault gouge at 150 MPa mean effective stress, *Pure Appl. Geophys.*, *142*, 749–775.
Shipboard Scientific Party (2001a), Leg 190 summary, *Proc. Ocean Drill. Program Initial Rep.*, *190*, 1–87, doi:10.2973/odp.proc.ir.190.101.2001.
Shipboard Scientific Party (2001b), Site 1174, *Proc. Ocean Drill. Program Initial Rep.*, *190*, 1–149, doi:10.2973/odp.proc.ir.190.105.2001.
Skempton, A. W. (1964), Long-term stability of clay slopes, *Geotechnique*, *14*, 77–102.
Solum, J. G., S. H. Hickman, D. A. Lockner, D. E. Moore, B. A. van der Pluijm, and J. P. Evans (2006), Mineralogical characterization of protolith and fault rocks from the SAFOD main hole, *Geophys. Res. Lett.*, *33*, L21314, doi:10.1029/2006GL027285.
Steurer, J. F., and M. B. Underwood (2003), Clay mineralogy of mudstones from the Nankai Trough reference sites 1173 and 1177 and frontal accretionary prism site 1174, *Proc. Ocean Drill. Program Initial Rep.*, *190/196*, 1–9, doi:10.2973/odp.proc.sr.190196.211.2003.
Takahashi, M., K. Mizoguchi, K. Kitamura, and K. Masuda (2007), Effects of clay content on the frictional strength and fluid transport property of faults, *J. Geophys. Res.*, *112*, B08206, doi:10.1029/2006JB004678.
Tembe, S., D. A. Lockner, J. G. Solum, C. A. Morrow, T.-F. Wong, and D. E. Moore (2006), Frictional strength of cuttings and core from SAFOD drillhole phases 1 and 2, *Geophys. Res. Lett.*, *33*, L23307, doi:10.1029/2006GL027626.
Tiwari, B., A.M. ASCE, and H. Marui (2005), A new method for the correlation of residual shear strength of the soil with mineralogical composition, *J. Geotech. Geoenviron. Eng.*, *31*(9), doi:10.1061/(ASCE)1090-0241(2005)131:9(1139).
Underwood, M. B. (2002), Strike-parallel variation in clay mineralogy, fault vergence, and up-dip limits to the seismogenic zone, *Geology*, *30*(2), 155–158.
Underwood, M. B., K. Pickering, J. M. Gieskes, M. Kastner, and R. Orr (1993) Sediment geochemistry, clay mineralogy, and diagenesis: A synthesis of data from Leg 131, Nanakai Trough, *Proc. Ocean Drill. Program Sci. Results*, *131*, 343–363.
Wilson, M. E. J., S. Hirano, C. L. Fergusson, J. Steurer, and M. B. Underwood (2003) Data report: Sedimentological and petrographic characteristics of volcanic ashes and siliceous claystones (altered ashes) from sites 1173, 1174, and 1177, Leg 190, *Proc. Ocean Drill. Program Sci. Results*, *190/196*, 1–9.
Zoback, M. D., and J. D. Byerlee (1976), Effect of high-pressure deformation on permeability of Ottawa Sand, *AAPG Bull.*, *60*, 1531–1542.

D. A. Lockner, U.S. Geological Survey, 345 Middlefield Rd., Menlo Park, CA 94025-3591, USA.

S. Tembe, Institute for Soil Mechanics and Rock Mechanics, Karlsruhe Institute of Technology, Karlsruhe D-76128, Germany. (sheryl.tembe@kit.edu)

T.-F. Wong, Department of Geosciences, State University of New York at Stony Brook, Stony Brook, NY 11790, USA.